

ATOMIC-TO-CONTINUUM MULTISCALE MODELING OF DEFECTS IN CRYSTALS WITH NONLOCAL ELECTROSTATIC INTERACTIONS*

PRASHANT K. JHA[†], JASON MARSHALL[§], JAROSLAW KNAP[¶], AND KAUSHIK DAYAL^{||}

Abstract. This work develops a multiscale modeling framework for defects in crystals with general geometries and boundary conditions in which ionic interactions are important, with potential application to, e.g., ionic solids and electric field interactions with materials. The overall strategy is posed in the framework of the Quasicontinuum multiscale method; specifically, the use of a finite-element inspired kinematic description enables a significant reduction in the large number of degrees of freedom to describe the atomic positions. The key advance of this work is a method for the efficient and accurate treatment of nonlocal electrostatic charge-charge interactions without restrictions on the geometry or boundary conditions. Electrostatic interactions are long-range with slow decay, and hence require consideration of all pairs of charges making a brute-force approach computationally prohibitive. The method proposed here accounts for the exact charge-charge interactions in the near-field and uses a coarse-grained approximation in the far-field. The coarse-grained approximation and the associated errors are rigorously derived based on the limit of a finite body with a small periodic lengthscale, thereby enabling the errors in the approximation to be controlled to a desired tolerance. The method is applied to a simple model of Gallium Nitride and it is shown that electrostatic interactions can be approximated with a desired level of accuracy using the proposed methodology.

1. Introduction. Electrostatic (Coulombic) interactions play a dominant role in the structure and response of materials of various classes, e.g., [1, 2, 3, 4, 5, 6, 7, 8, 9, 10, 11, 12, 13]. These interactions arise at the atomic scale in the interaction between electrons and protons. Therefore, understanding the response of materials, particularly the role of atomic-scale defects in determining material response, requires us to model materials starting from these scales. However, a key challenge in dealing with electrostatic interactions is that they are long-range; i.e., they decay slowly with distance and cannot be simply cut-off without serious qualitative errors [14]. Therefore, it is important to account for all charge-charge interactions in a given system, making it computationally expensive to deal with large atomic systems that are required to avoid spurious size-effects and spurious image defects.

Multiscale methods such as the quasicontinuum approach (QC) provide an efficient means of dealing with large atomic systems [15, 16, 17, 18, 19, 20, 21, 22, 23, 24, 25]. The ideas behind QC are inspired by the finite element method (FEM): an adaptive interpolation of atomic positions that preserves high resolution near defects and coarse-grains away from defects, and a quadrature rule to efficiently evaluate the total energy to enable minimization. However, a key requirement is that the quadrature rule uses local evaluations to be efficient, and therefore QC is currently restricted to short-range bonded interactions and cannot be used with long-range electrostatic interactions.

In this work, we build on [26] to formulate and demonstrate an efficient and accurate method that extends QC to account for long-range electrostatic interactions. The key idea is a controlled approach to coarse-grain electrostatic interactions – in terms of the polarization density – that enables us to perform efficient evaluations of the total energy. In contrast to [26] that applied this coarse-graining approximation even to charges that were close to each other, this work develops a hybrid approach that uses direct evaluations for charges that are close to each other while coarse-graining charge interactions over longer distances. This strategy is enabled by rigorous error bounds that we find here to enable us to appropriately choose the coarse-graining distance.

*November 15, 2022

[†]This material is declared a work of the U.S. Government and is not subject to copyright protection in the United States. Approved for public release; distribution is unlimited.

[‡]Oden Institute for Computational Engineering and Sciences, The University of Texas at Austin, Austin, TX 78712, USA. prashant.jha@austin.utexas.edu

[§]Northrop Grumman, 2980 Fairview Park Drive, Falls Church, VA 22042, USA. jason.p.marshall@gmail.com

[¶]Physical Modeling and Simulation Branch, FCDD-RLC-EM, U.S. Army Combat Capabilities Development Command, Army Research Laboratory, Aberdeen Proving Ground, MD, 21005-5066, USA. jaroslaw.knap@army.mil

^{||}Center for Nonlinear Analysis, Department of Mathematical Sciences, Carnegie Mellon University; Department of Mechanical Engineering, Carnegie Mellon University; Department of Civil and Environmental Engineering, Carnegie Mellon University, Pittsburgh, PA 15213, USA. Kaushik.Dayal@cmu.edu

Electrostatic Interactions in Materials. The electrostatic energy between charges q_i and q_j with separation distance r_{ij} is given by:

$$(1) \quad W = \frac{q_i q_j}{4\pi\epsilon_0 r_{ij}},$$

where ϵ_0 is the dielectric value of free space. This interaction energy is long-range: because of its slow $1/r$ decay, it gives rise to a divergent series when summed over many interacting charges of the same sign.

In ionic solids, while each repeating unit cell of the periodic crystal lattice is net charge neutral, there are positive and negative charges within the unit cell. The effective interactions energy goes as $1/r^3$, which is long-ranged in 3-d due to the conditionally-convergent nature of the total energy in a crystal lattice. In a finite crystal, the physical implication is that the energy converges slowly and we have to be careful in accounting for the far-field boundary conditions as well as not truncate the summation naively.

Metallic crystals, however, are different because the charge configuration – due to the presence of mobile electrons that can shield the long-range interactions – leads to effective electrostatic interactions that decay faster than $1/r^5$. In this setting, convergence of the energy summation is fast and can be truncated without significant error. Therefore, it is typical to combine the electrostatic interactions with the short-range bonded interactions rather than account for them separately.

A more detailed discussion of these issues can be found in [26].

Existing Methods for Electrostatic Interactions. A widely-used class of methods are Ewald summations [27, 28] and modifications of Ewald summations [29, 28]. These methods decompose the summation into a real-space part and a Fourier- / frequency- space part, both of which are individually fast to calculate. The real-space part accounts for the interactions within a small cutoff radius, while the frequency-space part accounts for the interactions outside the cutoff radius. The real-space calculation is fast because it involves only a few charges, and the frequency-space calculation is fast because it exploits periodicity and charge smearing. However, Ewald methods have significant limitations: first, it is restricted to infinite periodic crystals, and thus is not applicable to defects or inhomogeneously deformed crystals; and second, it is restricted to only the simplest electrical boundary conditions.

An elegant and powerful method for electrostatics is the fast multipole method (FMM) [30, 31, 32]. This method performs a Taylor series expansion of the electrostatic kernel about a cluster of charges, i.e., a multipole expansion. The method then calculates the higher-order moments from the cluster and approximates the net interaction with the resulting moments. The error in the method can be controlled based on the distance of a cluster from the point of interest and the number of moments included in the approximation. While it is able to deal with general charge configurations efficiently, i.e., a calculation that nominally scales with the square of the number of charges is reduced to a linear scaling, it does not account for potential efficiencies that arise when the charge configuration is close to periodic.

Another important method is the Reaction Field (RF) method [33, 34, 35]. This method is prominent in computational chemistry for molecules surrounded by a macroscopically-homogeneous liquid or solid. The electrostatic interactions are computed exactly within the molecule, and the far-field is accounted for by treating the surrounding medium as a homogeneous dielectric. The homogeneous dielectric responds to fields from the molecule by developing a polarization density, and thereby provides a “reaction field” on the molecule.

The Proposed Method. The proposed method is inspired by elements of the FMM and RF methods; however, it seeks to go beyond FMM by exploiting the near-periodicity of the charge configuration to be more efficient, and derive – rather than simply assume as in RF – the (possibly nonlinear) response of the coarse-grained medium.

Focusing on ionic solids, to compute the electric field at a atomic site, we consider a small neighborhood around a lattice site within which electric interactions are computed exactly, and outside of this neighborhood, we approximate the electrical interaction using a coarse-graining based on the polarization. We obtain an upper bound on the error due to this approximation and, through numerical examples, show that error can be controlled to within a desired tolerance by adjusting the neighborhood within which the interactions are computed exactly. This important feature of our work extends the method proposed in [26].

Our coarse-graining approach is based on methods from homogenization and discrete-to-continuum analyses. For example, in the context of electrical and magnetic interactions, continuum energies based on discrete-to-continuum approaches are obtained for a system of discrete dipoles on a periodic 3-d lattice [36, 37, 10, 38, 39, 40] as well as for

topologically low-dimensional materials [41]. We combine these coarse-graining strategies for electrical interactions with the framework of QC. QC provides a systematic framework to reduce the number of atomic degree of freedoms. In brief, only a small subset of atoms – called *representative atoms* – are allowed to displace independently, while the positions of the other atoms – *ghost atoms* – are constrained by the motion of the representative atoms through interpolation. The representative atoms are chosen adaptively: where there are rapid variations, the representative atom distribution is finer, and coarser elsewhere. To minimize the energy, we require the derivatives of the total energy with respect to the displacement of the representative atoms; physically, this corresponds to the net force on the atom. To compute these forces efficiently, QC methods use the cluster summation approximation [19, 42, 43, 24]. In this work, we adapt the cluster summation approach to account for long-range electrostatic forces.

Organization. Section 2 presents the formulation of the atomic system as a multi-lattice. Section 3 reviews briefly the QC method. Section 4 describes the approximation of long-range electrostatic interactions and how this fits into the QC method. Section 5 describes key aspects of the implementation. Section 6 presents numerical results that highlight the accuracy and efficiency of the method. Section 7 provides concluding remarks.

Notation. We denote the sets of real, integers, and natural numbers by $\mathbb{R}, \mathbb{Z}, \mathbb{N}$, respectively. The set of natural numbers bounded above by an integer $M \geq 1$ is denoted by \mathbb{N}_M , i.e., $\mathbb{N}_M = \mathbb{N} \cap [1, M]$. Further, \mathbb{R}^d and \mathbb{Z}^d denote the d -dimensional real and integer spaces, respectively. The ambient space is assumed to be \mathbb{R}^3 and the dimension of the atomic system and ambient space are assumed to be same. We denote the standard orthonormal basis of \mathbb{R}^3 by $\{e_1, e_2, e_3\}$. Bold letters will be used to denote the vector and tensor quantities; $\mathbf{x} = (x_1, x_2, x_3) \in \mathbb{R}^3$ denotes a point, $\mathbf{i} = (i_1, i_2, i_3) \in \mathbb{Z}^3$ an integer vector, and $\mathbf{A} = [A_{ij}] \in \mathbb{R}^{3 \times 3}$ a second order tensor. Here, the representation of \mathbf{x} and \mathbf{A} are in orthonormal basis $\{e_1, e_2, e_3\}$. The Euclidean norm of \mathbf{x} is denoted by $|\mathbf{x}|$, i.e., $|\mathbf{x}| = \sqrt{x_i x_i}$; we will use Einstein summation convention except when stated. The norm of a tensor \mathbf{A} is $|\mathbf{A}| = \sqrt{\mathbf{A} : \mathbf{A}}$, where $\mathbf{A} : \mathbf{B} = A_{ij} B_{ij}$. Given a generic function $f: U \rightarrow V$, we will use the notation $f(A)$, for $A \subset U$, to denote the image of a set A , i.e., $f(A) = \{f(a) : a \in A\}$. We denote the empty set by \emptyset .

We list general notation in Table 1 and notation specific to QC in Table 2.

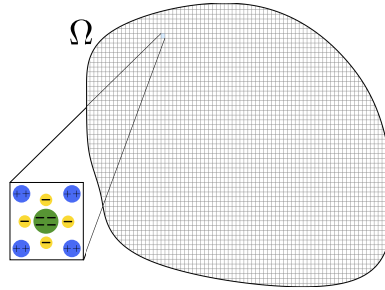


Fig. 1: A finite crystalline material Ω with several charged species in each unit cell.

2. Formulation of an atomic system as a lattice with multiple species.

2.1. Kinematics. Consider a general multilattice crystal system with $M \geq 1$ number of species per unit cell in 3-d Euclidean space \mathbb{R}^3 . Figure 1 shows a schematic of a finite crystalline material Ω wherein each unit cell (or lattice site) contains several charged species. Figure 2 shows an idealization as a multilattice. The multilattice is obtained by translating a base lattice (say, corresponding to the first species) by some amount and superposing the translated lattice. Denoting by $\mathbf{i} \in \mathbb{Z}^3$ the triplet integer uniquely identifying a site in the base lattice, and by $\{\mathbf{a}_1, \mathbf{a}_2, \mathbf{a}_3\}$ the Bravais lattice vectors, then the reference position of a lattice site is given by:

$$(2) \quad \bar{\mathbf{X}}_{\mathbf{i}} = \sum_{k=1}^3 i_k \mathbf{a}_k.$$

Table 1: General notation.

M	Number of species per unit cell, or equivalently number of lattices in a multilattice
$I = (\mathbf{i}, \alpha) \in \mathbb{Z}^3 \times \mathbb{N}_M$	Integer tuple uniquely identifying an atom in a multilattice; $\mathbf{i} \in \mathbb{Z}^3$ identifies the unit cell and $\alpha \in \mathbb{N}_M$ gives the species
$L \subset \mathbb{Z}^3 \times \mathbb{N}_M$	Set of indices of all atoms in a multilattice
$\boldsymbol{\eta}: L \rightarrow \mathbb{Z}^3$	The map that identifies the unit cell given an atom; $\boldsymbol{\eta}(I) = \mathbf{i}$ for $I = (\mathbf{i}, \alpha) \in L$
$\kappa: L \rightarrow \mathbb{N}_M$	The map that identifies the species given an atom; $\kappa(I) = \alpha$ for $I = (\mathbf{i}, \alpha) \in L$
$\bar{L} = \boldsymbol{\eta}(L)$	Indices of all unit cells in a multilattice, where $\boldsymbol{\eta}(L) = \{\boldsymbol{\eta}(I) : I \in L\}$
L_α	Indices of all lattice sites in α^{th} lattice in a multilattice, i.e., $L_\alpha = \{(\mathbf{i}, \alpha) : \mathbf{i} \in \bar{L}\}$
$\mathbf{X}_I, \mathbf{x}_I, \mathbf{u}_I := \mathbf{x}_I - \mathbf{X}_I$	Reference position, current position, and displacement of an atom $I \in L$, respectively
$\bar{\mathbf{X}}_{\mathbf{i}}, \bar{\mathbf{x}}_{\mathbf{i}}$	Reference and current position of site \mathbf{i} in a base lattice, respectively
$\mathbf{Y}_\alpha, \mathbf{y}_\alpha$	Reference and current position of α -species relative to the lattice site's reference and current position, respectively
$U_{\mathbf{i}}$	Unit cell associated with a lattice site $\mathbf{i} \in \bar{L}$
$\mathbf{p}_{\mathbf{i}}$	Dipole density at a lattice site $\mathbf{i} \in \bar{L}$
q_I	Charge of species I ; $q_I = \hat{q}_{\kappa(I)} \in \{\hat{q}_{\mathbf{i}}\}_{\mathbf{i}=1}^M$
$\mathbf{X}(A), \mathbf{x}(A), \mathbf{u}(A)$	Vector of reference and current position, and displacement of atoms in a set A , respectively; e.g., $\mathbf{X}(A) = \{\mathbf{X}_I : I \in A\}$
$\Pi^{\text{in}}, W^{\text{ex}}, \Pi$	Stored energy, external working, and total potential energy of the atomic system L , respectively
$\Pi^{\text{sr}}, \Pi^{\text{el}}$	Stored energy contributions due to short-range and electrostatic interactions, respectively
$\mathbf{f}_I^{\text{in}}, \mathbf{f}_I^{\text{ex}}, \mathbf{f}_I$	Internal, external, and total force acting on an atom I , respectively
$\mathbf{f}^{\text{in}}(A), \mathbf{f}^{\text{ex}}(A), \mathbf{f}(A)$	Vector of internal, external, and total force acting on atoms in a set A , respectively; e.g., $\mathbf{f}^{\text{in}} = \{\mathbf{f}_I^{\text{in}} : I \in A\}$
$\mathbf{E} = \mathbf{E}(\mathbf{x}), \rho = \rho(\mathbf{x})$	Electric field and charge density, $\mathbf{x} \in \mathbb{R}^3$

Within a unit cell at site \mathbf{i} , there are M atoms; to identify atoms uniquely, we use a multi-index $I = (\mathbf{i}, \alpha)$, where $\mathbf{i} \in \mathbb{Z}^3$ gives the site and $\alpha \in \mathbb{N}_M$ gives the atomic species type. Denoting by $\mathbf{s}_I, I \in \mathbb{Z}^3 \times \mathbb{N}_M$, the reference position of atom I relative to the reference position $\bar{\mathbf{X}}_{\mathbf{i}}$ of lattice site \mathbf{i} , the reference position of an atom I is simply

$$(3) \quad \mathbf{X}_I = \bar{\mathbf{X}}_{\mathbf{i}} + \mathbf{s}_I.$$

The shift vector \mathbf{s}_I does not vary from site to site, and, therefore, we have $\mathbf{s}_I = \hat{\mathbf{s}}_{\kappa(I)} \in \{\hat{\mathbf{s}}_\alpha\}_{\alpha=1}^M$. Further, without loss of generality, we let $\hat{\mathbf{s}}_1 = \mathbf{0}$ so that the location of the atom of species $\alpha = 1$ coincides with the location of the corresponding lattice site, i.e.,

$$\mathbf{X}_{(\mathbf{i}, 1)} = \bar{\mathbf{X}}_{\mathbf{i}}.$$

Table 2: QC notation.

$L_\alpha^r, L_\alpha^g \subset L_\alpha$	Representative (rep.) and ghost atoms in α -lattice, respectively
$L^r, L^g \subset L$	Rep. and ghost atoms in a multilattice, respectively; for $a \in \{r, g\}$, $L^a = \bigcup_{\alpha=1}^M L_\alpha^a$
$\mathcal{T}(\mathbf{X}(L_\alpha^r))$	Triangulation with rep. atoms in α -lattice
$\mathcal{N}_I = \mathcal{N}_I(\mathbf{x})$	Shape function associated with the rep. atom $I \in L^r$
$\Pi^{r,in}, W^{r,ex}, \Pi^r$	Stored energy, external working, and total potential energy as a function of displacement of rep. atoms, respectively
f_I^r, f_I^g	Any quantity (scalar or vector) f_I specific to the rep. and ghost atoms, respectively. E.g., \mathbf{X}_I^r and \mathbf{X}_I^g refers to the reference position of rep. atom $I \in L^r$ and ghost atom $I \in L^g$
$\mathbf{f}^r, \mathbf{f}^g$	Vectorial quantity \mathbf{f} specific to the rep. and ghost atoms, respectively. E.g., \mathbf{X}^r and \mathbf{X}^g refers to the vector of reference positions of all rep. and ghost atoms
Ω^{at}, Ω^{co}	Atomistic and coarse-grained regions respectively; in the atomistic region, all atoms are rep. atoms
$\bar{L}^{at}, \bar{L}^{co}$	Set of lattice sites in atomistic Ω^{at} and coarse-grained Ω^{co} regions, respectively

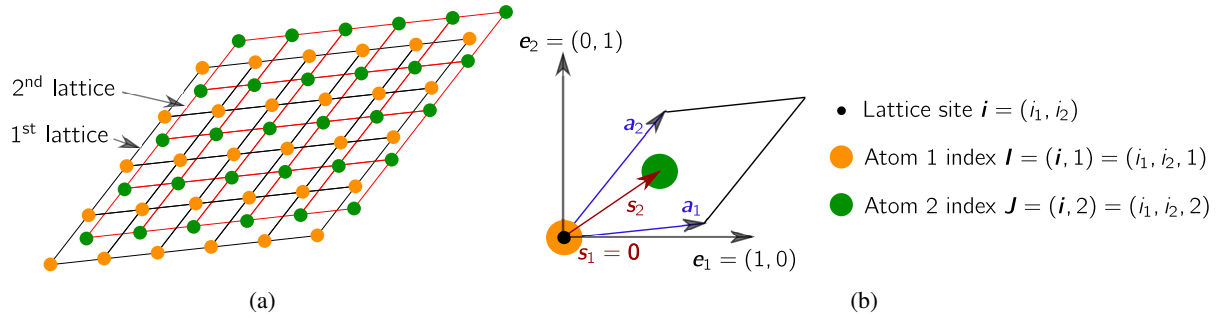


Fig. 2: Schematic example of a two-dimensional multilattice.

Given a domain $\Omega \subset \mathbb{R}^3$, we define the indices of the atoms in a multilattice within Ω as follows:

$$(4) \quad L = \{I = (\mathbf{i}, \alpha) \in \mathbb{Z}^3 \times \mathbb{N}_M : \mathbf{X}_I \in \Omega\}.$$

We also define the set of indices of sites in a base lattice and indices of atoms in α -lattice, $\alpha = 1, 2, \dots, M$. We set:

$$(5) \quad \bar{L} = \{\eta(I) : I \in L\}, \quad L_\alpha = \{I = (\mathbf{i}, \alpha) : \mathbf{i} \in \bar{L}\}.$$

For each site $\mathbf{i} \in \bar{L}$, we define a unit cell $U_{\mathbf{i}}$ as follows

$$(6) \quad U_{\mathbf{i}} = \left\{ \mathbf{x} = \bar{\mathbf{X}}_{\mathbf{i}} + \sum_{k=1}^3 r_k \mathbf{a}_k : r_k \in [0, 1), k = 1, 2, 3 \right\}$$

Given an atom $I \in L$, we can identify the lattice site by $\eta(I)$ and an associated unit cell by $U_{\eta(I)}$. For future reference, we note that

$$(7) \quad \begin{aligned} 0 \leq |\mathbf{y}| &\leq \hat{c}l, & \forall \mathbf{y} \in U_{\mathbf{0}}, \\ 0 \leq |\boldsymbol{\xi}| &\leq \hat{c}, & \forall \boldsymbol{\xi} \in \frac{U_{\mathbf{0}}}{l} = \{\mathbf{y}/l : \mathbf{y} \in U_{\mathbf{0}}\}, \end{aligned}$$

for some constant $\hat{c} = O(1)$. Further, $\text{diam}(U_{\mathbf{0}}) = l\hat{c} = l \text{diam}(\tilde{U}_{\mathbf{0}}/l)$.

We use $q_I = \hat{q}_{\kappa(I)}$ to denote the effective charge of species I , where \hat{q}_{α} is the effective charge of species type α , $\alpha = 1, 2, \dots, M$.

2.2. Energies and Forces. In this work, we will consider deformations that are minimizers of the energy. This corresponds to zero temperature.

We use \mathbf{x}_I and \mathbf{u}_I to denote the current position and the displacement, respectively, of an atom $I \in L$. It is also convenient to write the locations of the atoms in a unit cell relative to the position of the site. We will use the notation $\bar{\mathbf{x}}_i$ to denote the current position of site $i \in \bar{L}$. Relative to the reference and current position of a site i , we define the reference and current position of an atom of α type in a unit cell U_i by \mathbf{Y}_{α} and \mathbf{y}_{α} , respectively, with these quantities implicitly dependent on i .

The working by the external forces $\mathbf{f}^{ex}(L) = \{\mathbf{f}_I^{ex} : I \in L\}$ is:

$$(8) \quad W^{ex}(\mathbf{u}(L)) = \sum_{I \in L} \mathbf{f}_I^{ex} \cdot \mathbf{u}_I,$$

where $\mathbf{u}(L) = \{\mathbf{u}_I : I \in L\}$. Let $\Pi^{in}(\mathbf{u}(L))$ denote the stored energy; the specific form will be discussed momentarily. Then the total potential energy is $\Pi = \Pi^{in} - W^{ex}$.

The configuration of the atomic system under a system of loads is given by

$$\frac{\partial \Pi(\mathbf{u}(L))}{\partial \mathbf{u}(L)} = \mathbf{0}$$

or, in expanded form,

$$(9) \quad \frac{\partial \Pi(\mathbf{u}(L))}{\partial \mathbf{u}_I} = \mathbf{0}, \quad \forall I \in L.$$

We note that, from (8),

$$(10) \quad \frac{\partial W^{ex}(\mathbf{u}(L))}{\partial \mathbf{u}_I} = \mathbf{f}_I^{ex}.$$

If we define the internal force at atom I as:

$$(11) \quad \mathbf{f}_I^{in} := -\frac{\partial \Pi^{in}(\mathbf{u}(L))}{\partial \mathbf{u}_I}$$

then the equation for the equilibrium configuration is:

$$(12) \quad \mathbf{f}_I := -\frac{\partial \Pi}{\partial \mathbf{u}_I} = \mathbf{f}_I^{in}(\mathbf{u}(L)) + \mathbf{f}_I^{ex} = \mathbf{0}, \quad \forall I \in L.$$

The specific form of force \mathbf{f}_I^{in} depends on the interatomic potential. From fundamental quantum mechanical models of matter, we can decompose Π^{in} into the sum of the short-range pairwise interatomic interaction, Π^{sr} , and the electrostatic interaction, Π^{el} :

$$(13) \quad \Pi^{in}(\mathbf{u}(L)) = \Pi^{sr}(\mathbf{u}(L)) + \Pi^{el}(\mathbf{u}(L)).$$

We next describe these interactions in further detail.

Short-range interaction. In general, short-range interactions between atoms are nonlinear and multibody and cannot typically be uniquely decomposed into an energy per atom or energy per lattice site [17]. However, under the assumption that the interactions are short-range and that the lattice is locally periodic, there is a well-defined notion of an energy per lattice site.

As an illustrative example, we consider a widely used and general short-range interaction model, referred to as the Embedded Atom Method (EAM) [44, 45, 46]. In EAM, we can decompose the stored energy Π^{sr} into contributions from individual atoms Π_I^{sr} , and the individual energies have the form:

$$(14) \quad \Pi_I^{sr}(\mathbf{u}(L)) = \frac{1}{2} \sum_{J \in N_I^{pw}, J \neq I} \Phi_{\kappa(I)\kappa(J)}(|\mathbf{x}_I - \mathbf{x}_J|) + \mathcal{F}(\rho_I^{eam}),$$

where the first term is due to pairwise interaction of an atom I with neighboring atoms in N_I^{pw} and the second term is the energy of an atom I due to local electron density ρ_I^{eam} . Here, $\Phi_{\alpha\beta}(r)$, $1 \leq \alpha, \beta \leq M$, are the pairwise interatomic potentials parameterized by the species types. For example, in Gallium Nitride (GaN) (Ga – 1 and N – 2), Φ_{11} , Φ_{22} , and Φ_{12} correspond to two Ga atoms interacting, two N atoms interacting, and one Ga and one N atoms interacting, respectively.

The local electron density ρ_I^{eam} in EAM is assumed to be:

$$(15) \quad \rho_I^{eam}(\mathbf{u}(L)) = \sum_{J \in N_I^{eam}, J \neq I} g_{\kappa(I)\kappa(J)}(|\mathbf{x}_I - \mathbf{x}_J|),$$

where N_I^{eam} is the list of neighboring atoms, and $g_{\kappa(I)\kappa(J)}(|\mathbf{x}_I - \mathbf{x}_J|)$ is the effective electron density at atom I due to atom J and is parameterized by the species.

The stored energy due to short-range interaction is $\Pi^{sr} = \sum_{I \in L} \Pi_I^{sr}$. The internal force \mathbf{f}_I^{sr} at atom I is given by

$$(16) \quad \begin{aligned} \mathbf{f}_I^{sr} &= -\frac{\partial \Pi^{sr}}{\partial \mathbf{u}_I} = -\sum_{J \in L} \frac{\partial \Pi_J^{sr}}{\partial \mathbf{u}_I} \\ &= \sum_{J \in N_I^{pw}, J \neq I} \Phi'_{\kappa(I)\kappa(J)}(|\mathbf{x}_I - \mathbf{x}_J|) \frac{\mathbf{x}_J - \mathbf{x}_I}{|\mathbf{x}_J - \mathbf{x}_I|} \\ &\quad + \sum_{J \in N_I^{eam}, J \neq I} (\mathcal{F}'(\rho_I^{eam}) + \mathcal{F}'(\rho_J^{eam})) g'_{\kappa(I)\kappa(J)}(|\mathbf{x}_I - \mathbf{x}_J|) \frac{\mathbf{x}_J - \mathbf{x}_I}{|\mathbf{x}_J - \mathbf{x}_I|}, \end{aligned}$$

where $\Phi'_{\alpha\beta} = d\Phi_{\alpha\beta}/dr$ and $g'_{\alpha\beta} = dg_{\alpha\beta}/dr$.

Electrostatic interaction. An important feature of electrostatic interactions is that, while long-range, they are pairwise between charges and energies/forces can be superposed. We assume that the species in a multilattice carry effective charges but that each unit cell is charge-neutral:

$$(17) \quad \sum_{\alpha=1}^M \hat{q}_{\alpha} = 0.$$

Alternatively, we could consider a charge-density field $\rho(\mathbf{x})$ satisfying:

$$(18) \quad \begin{aligned} \text{(charge neutrality)} \quad & \int_{U_{\mathbf{i}}} \rho(\mathbf{y}) \, d\mathbf{y} = 0, \quad \forall \mathbf{i} \in \mathbb{Z}^3, \\ \text{(periodicity)} \quad & \rho(\bar{\mathbf{X}}\mathbf{i} + \mathbf{y}) = \rho(\mathbf{y}), \quad \forall \mathbf{i} \in \mathbb{Z}^3, \forall \mathbf{y} \in U_0. \end{aligned}$$

Using the Dirac delta function $\delta(\mathbf{x})$, discrete charges can be represented through a charge density field by defining $\rho(\mathbf{x}) = \sum_{I \in \bar{L}} q_I \delta_{\mathbf{x}_I}(\mathbf{x})$.

The energy of atom I due to electrostatic interactions is given by

$$(19) \quad \Pi_I^{el}(\mathbf{u}(L)) = \frac{1}{2} \sum_{J \in L, J \neq I} \frac{q_I q_J}{4\pi\epsilon_0} \frac{1}{|\mathbf{x}_I - \mathbf{x}_J|}$$

and the stored energy due to electrostatic interactions is $\Pi^{el}(\mathbf{u}(L)) = \sum_{I \in L} \Pi_I^{el}(\mathbf{u}(L))$. The force due to electrostatic interactions on atom I is

$$(20) \quad \mathbf{f}_I^{el} = -\frac{\partial \Pi^{el}}{\partial \mathbf{u}_I} = q_I \left[\sum_{J \in L, J \neq I} \frac{q_J}{4\pi\epsilon_0} \frac{\mathbf{x}_I - \mathbf{x}_J}{|\mathbf{x}_I - \mathbf{x}_J|^3} \right] = q_I \mathbf{E}(\mathbf{x}_I),$$

where we have introduced the electric field $\mathbf{E}(\mathbf{x})$ as a function of the spatial position $\mathbf{x} \in \mathbb{R}^3$ given by

$$(21) \quad \mathbf{E}(\mathbf{x}) = \sum_{J \in L, \mathbf{x}_J \neq \mathbf{x}} \frac{q_J}{4\pi\epsilon_0} \frac{\mathbf{x} - \mathbf{x}_J}{|\mathbf{x} - \mathbf{x}_J|^3}.$$

REMARK 2.1. *The long-range interactions are challenging since the expense of computing the forces goes as N^2 , where N is the number of charges. In contrast, the cost of computing the forces due to short-range interactions goes as nN , where $n \ll N$ for large systems and is related to the number of atoms within the short-range interaction cut-off.*

3. Quasicontinuum method. The Quasicontinuum (QC) method is a powerful tool for solving large atomistic problems. The method was originally developed in [20]. Since then multiple versions of the method have been developed, and have been reviewed in [15, 16]. For this work we use the QC method proposed in [19] and its generalization to multi-lattice system in [21]; these QC methods are capable of fully resolving parts of the system – near defects and other regions where atomic resolution is essential – while coarse-graining in the parts where the deformation varies slowly. However, [19] did not account for long-range electrostatic interactions, while [21] used Ewald summations that are very restrictive in the assumptions on the nature of electric fields. In [26], electrostatic interactions in generality were included but it used a coarse-graining approximation – based on the Cauchy-Born rule – in the entire system, including at defects. However, this is too crude of an approximation and is inaccurate in modeling defects, which can provide most of the interesting behavior.

If the domain of interest Ω is large, i.e., $\text{diam}(\Omega) \gg l$, where l is the lattice size and is of the order of 0.1 nanometer, (12) is computationally intractable due to the very large number of atoms in the system. This difficulty is even more formidable when dealing with a long-range electrostatic interactions. The QC method overcomes this difficulty by selecting a much smaller subset of atoms, so-called *representative atoms* (rep. atoms, in brief), from the full set of atomic degrees of freedom. The remaining atoms, referred to as *ghost atoms*, are constrained to deform based on the deformation of rep. atoms. As a result, the number of equations in (9) is reduced to $n \ll N$, where n is the number of rep. atoms and N is the total number of atoms. Typically, near the defect or other regions with rapidly-varying deformation, all atoms are selected as rep. atoms to achieve full atomic resolution; we refer to this region $\Omega^{at} \subset \Omega$ as the atomistic region (Figure 3). As we move away from the atomistic region, we can progressively select fewer atoms as rep. atoms. In $\Omega^{co} = \Omega \setminus \Omega^{at}$ – referred to as coarse-grained region – only a small fraction of atoms are selected as rep. atoms and the remaining atoms are treated as ghost atoms. The positions of the ghost atoms are obtained by using the shape functions to interpolate between the positions of the rep. atoms. Lattice sites in Ω^{co} are collected in \bar{L}^{co} while the sites in Ω^{at} are collected in \bar{L}^{at} .

Suppose L_α^r and L_α^g are the rep. and ghost atoms in the α -lattice, respectively, such that $L_\alpha = L_\alpha^r \cup L_\alpha^g$, $L_\alpha^r \cap L_\alpha^g = \emptyset$. We denote the convex hull consisting of tetrahedrons by $\mathcal{T}(\mathbf{X}(L_\alpha^r))$ given the reference coordinates $\mathbf{X}(L_\alpha^r)$ of the rep. atoms. Let $\mathcal{N}_I(\mathbf{x})$ denote the shape function for a rep. atom $I \in L_\alpha^r$. The interpolation functions satisfy the following properties:

$$(22) \quad \begin{aligned} & \text{(0-1 property)} \quad \mathcal{N}_I(\mathbf{X}_J) = \delta_{IJ}, \quad I, J \in L_\alpha^r, \\ & \text{(partition of unity)} \quad \sum_{J \in L_\alpha^r} \mathcal{N}_J(\mathbf{x}) = 1, \quad \forall \mathbf{x} \in \cup_{T \in \mathcal{T}(\mathbf{X}(L_\alpha^r))} \bar{T}. \end{aligned}$$

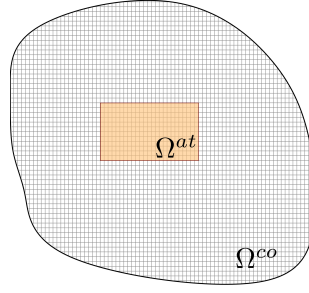


Fig. 3: Partition of the domain Ω into the atomistic region Ω^{at} and the coarse-grained region Ω^{co} . In Ω^{at} , all atoms are selected as rep. atoms while in Ω^{co} , a small subset of atoms are selected as rep. atoms to reduce the dimensionality of the problem. The displacement of the ghost atoms in Ω^{co} are obtained by interpolating the displacement of the rep. atoms.

Further, we assume that each lattice is interpolated independently, and therefore the operation $\mathcal{N}_I(\mathbf{X}_J)$ is defined only if $\kappa(I) = \kappa(J)$. This allows us to geometrically decouple the lattices: the shape functions of the rep. atoms of the α -lattice depends on the rep. atoms of that lattice, and the ghost atoms of the α -lattice are interpolated based on the rep. atoms of the same lattice, i.e., the α -lattice.

By combining the rep. and ghost atoms of all lattices, we get the set of rep. and ghost atoms in a multilattice system: $L^r = \cup_{\alpha=1}^M L_{\alpha}^r$ and $L^g = \cup_{\alpha=1}^M L_{\alpha}^g$.

If $\{\mathbf{u}_I^r\}_{I \in L_{\alpha}^r}$ are the displacements of all the rep. atoms in the α -lattice, then the displacement \mathbf{u}_I^g of a ghost atom $I \in L_{\alpha}^g$ is given by

$$(23) \quad \mathbf{u}_I^g = \sum_{J \in L_{\alpha}^r} \mathcal{N}_J(\mathbf{X}_I^g) \mathbf{u}_J^r.$$

That is, the displacement of the ghost atoms are obtained by interpolation using the shape functions and the rep. atom displacements. With (22), the equation above can be rewritten as follows, for any $I \in L$,

$$(24) \quad \mathbf{u}_I = \sum_{J \in L^r} \mathcal{N}_J(\mathbf{X}_I) \mathbf{u}_J^r = \sum_{J \in L_{\kappa(I)}^r} \mathcal{N}_J(\mathbf{X}_I) \mathbf{u}_J^r = \begin{cases} \mathbf{u}_I^g & \text{if } I \in L^g, \\ \mathbf{u}_I^r & \text{if } I \in L^r, \end{cases}$$

where the second equality is due to the fact that the lattices are interpolated independently. Other quantities such as the current position \mathbf{x}_I can be related to the position of the rep. atoms in a similar fashion.

We can now write the energies, Π and Π^{in} , and the external working, W^{ex} , as functions of the rep. atom positions. For example, by combining (8) and (24), the external working in terms of the displacements of the rep. atoms can be written:

$$(25) \quad W^{r,ex}(\mathbf{u}(L^r)) = W^{ex}(\mathbf{u}(L)) = \sum_{I \in L^r} \mathbf{f}_I^{r,ex} \cdot \mathbf{u}_I^r,$$

where $\mathbf{f}_I^{r,ex}$ is the external force acting on the rep. atom $I \in L^r$, and is given by

$$(26) \quad \mathbf{f}_I^{r,ex} = \sum_{J \in L} \mathbf{f}_J^{ex} \mathcal{N}_I(\mathbf{X}_J) = \sum_{J \in L_{\kappa(I)}} \mathbf{f}_J^{ex} \mathcal{N}_I(\mathbf{X}_J),$$

where we again used the fact that the lattices are interpolated independently. Here, $\{\mathbf{f}_I^{ex}\}_{I \in L}$ are the external forces acting on atoms. The stored energy $\Pi^{r,in}$, as a function of the displacement of the rep. atoms, can be written as

$$(27) \quad \Pi^{r,in}(\mathbf{u}(L^r)) = \Pi^{in}(\mathbf{u}(L)).$$

Combining this with (24) results in the following expression for the internal force, $\mathbf{f}_I^{r,in}$, acting on the rep. atom $I \in L^r$:

$$(28) \quad \mathbf{f}_I^{r,in} = -\frac{\partial \Pi^{r,in}(\mathbf{u}(L^r))}{\partial \mathbf{u}_I^r} = -\frac{\partial \Pi^{in}(\mathbf{u}(L))}{\partial \mathbf{u}_I^r} = \sum_{J \in L} \mathbf{f}_J^{in} \mathcal{N}_I(\mathbf{X}_J) = \sum_{J \in L_{\kappa(I)}} \mathbf{f}_J^{in} \mathcal{N}_I(\mathbf{X}_J).$$

From (28), we see that computing the internal force on the rep. atoms requires computing the forces on all the atoms. This is a significant limitation when dealing with a large number of atoms. Therefore, we consider a *cluster-based summation approximation*, following [19], to compute the internal forces on the rep. atoms efficiently. Consider a sum $S = \sum_{I \in L_\alpha} g_I$, where g_I is any quantity associated with atom $I \in L$. In a cluster-based summation approximation, the sum S is approximated as follows:

$$(29) \quad S \approx \sum_{I \in L_\alpha^r} w_I \left(\sum_{J \in C_I^r} g_J \right),$$

where $\{w_I\}_{I \in L_\alpha^r}$ are the weights, and $C_I^r, I \in L_\alpha^r$, is the set of atoms in the neighborhood of an atom I , i.e., a cluster set of the rep. atom I . In (29), the weights w_I are selected so that the summation approximation is exact for all shape functions \mathcal{N}_I . Note that, for $I \in L_\alpha^r$, C_I^r only consists of atoms in the α -lattice, i.e., $C_I^r \subset L_\alpha$. This is because the lattices are assumed to be interpolated independently. It is also assumed that any atom $J \in L$ can, at most, be a cluster atom of one rep. atom. As the size of the cluster C_I^r increases to have more atoms, the approximation (29) will be more accurate and more computationally expensive.

Using the cluster-based summation approximation, we can write (26) and (28) as:

$$(30) \quad \begin{aligned} \mathbf{f}_I^{r,ex} &\approx \sum_{J \in L_{\kappa(I)}^r} w_I \left(\sum_{K \in C_J^r} \mathbf{f}_K^{ex} \mathcal{N}_I(\mathbf{X}_K) \right), \\ \mathbf{f}_I^{r,in} &\approx \sum_{J \in L_{\kappa(I)}^r} w_I \left(\sum_{K \in C_J^r} \mathbf{f}_K^{in} \mathcal{N}_I(\mathbf{X}_K) \right). \end{aligned}$$

Governing equations in QC. The equilibrium equations are obtained by minimizing the total potential energy $\Pi^r(\mathbf{u}(L^r)) = \Pi^{r,in}(\mathbf{u}(L^r)) - W^{r,ex}(\mathbf{u}(L^r))$, to get:

$$(31) \quad \mathbf{f}_I^r = \mathbf{f}_I^{r,in}(\mathbf{u}(L^r)) + \mathbf{f}_I^{r,ex} = \mathbf{0}, \quad \forall I \in L^r.$$

Clearly, in solving (31), the major task is computing the internal force \mathbf{f}_K^{in} at some atom $K \in L$. We have

$$(32) \quad \mathbf{f}_K^{in} = \mathbf{f}_K^{sr} + \mathbf{f}_K^{el},$$

where the first contribution is due to the short-range interaction of an atom K with the neighboring atoms, and the second contribution is due to the electrostatic interaction. Because short-range forces have been extensively studied within the QC framework, we will not discuss the calculation of short-range forces in this paper. We focus on including the long-range electrostatic interactions in the QC method in the next section.

4. Approximation of the electrostatic interaction in the quasicontinuum framework. The force on an atom $I = (i, \alpha) \in L$ due to the charge-charge interaction can be written, following (20) and (21), as:

$$(33) \quad \mathbf{f}_I^{el} = q_I \mathbf{E}(\mathbf{x}_I) = q_I \left[\sum_{J \in L, \mathbf{x}_J \neq \mathbf{x}_I} \frac{q_J}{4\pi\epsilon_0} \frac{\mathbf{x}_I - \mathbf{x}_J}{|\mathbf{x}_I - \mathbf{x}_J|^3} \right] = \hat{q}_\alpha \left[\sum_{j \in \bar{L}} \sum_{\beta \in \mathbb{N}_M, \mathbf{x}_{(j,\beta)} \neq \mathbf{x}_I} \frac{\hat{q}_\beta}{4\pi\epsilon_0} \frac{\mathbf{x}_I - \bar{\mathbf{x}}_j - \mathbf{y}_\beta}{|\mathbf{x}_I - \bar{\mathbf{x}}_j - \mathbf{y}_\beta|^3} \right],$$

where we note that $\mathbf{X}_{(j,\beta)} = \bar{\mathbf{x}}_j + \mathbf{y}_\beta$, as $\bar{\mathbf{x}}_j$ gives the current position of lattice site j and \mathbf{y}_β gives the current position of species β relative to $\bar{\mathbf{x}}_j$. Further, we used that $q_I = \hat{q}_{\kappa(I)}$ for any $I \in L$. We focus on computing the electric field $\mathbf{E}(\mathbf{x})$ at any given location \mathbf{x} , and the force \mathbf{f}_I^{el} follows from $\mathbf{E}(\mathbf{x})$ easily.

4.1. Contribution from a single unit cell. We start with the contribution to $\mathbf{E}(\mathbf{x})$ from a single unit cell associated with a lattice site $\mathbf{j} \in \bar{L}$ as shown in Figure 4. Denoting by $\mathbf{E}_j(\mathbf{x})$ the electric field at \mathbf{x} due to the charges within the unit cell U_j , we have

$$(34) \quad \mathbf{E}_j(\mathbf{x}) = \sum_{\beta \in \mathbb{N}_M, \mathbf{x}_{(j,\beta)} \neq \mathbf{x}} \frac{\hat{q}_\beta}{4\pi\epsilon_0} \frac{\mathbf{x} - \bar{\mathbf{x}}_j - \mathbf{y}_\beta}{|\mathbf{x} - \bar{\mathbf{x}}_j - \mathbf{y}_\beta|^3}.$$

Instead of discrete charges $\{\hat{q}_\alpha\}$, if we consider the charge density field $\rho(\mathbf{x})$, \mathbf{E}_j can be expressed as

$$(35) \quad \mathbf{E}_j(\mathbf{x}) = \int_{U_j} \frac{\rho(\mathbf{z})}{4\pi\epsilon_0} \frac{\mathbf{x} - \mathbf{z}}{|\mathbf{x} - \mathbf{z}|^3} d\mathbf{z} = \int_{U_0} \frac{\rho(\bar{\mathbf{x}}_j + \mathbf{y})}{4\pi\epsilon_0} \frac{\mathbf{x} - \bar{\mathbf{x}}_j - \mathbf{y}}{|\mathbf{x} - \bar{\mathbf{x}}_j - \mathbf{y}|^3} d\mathbf{y} = - \int_{U_0} \rho(\bar{\mathbf{x}}_j + \mathbf{y}) \nabla g(\mathbf{x} - \bar{\mathbf{x}}_j - \mathbf{y}) d\mathbf{y},$$

where we have introduced a function $g(\mathbf{x})$ defined as

$$(36) \quad g(\mathbf{x}) = \frac{1}{4\pi\epsilon_0 |\mathbf{x}|},$$

with $\nabla g(\mathbf{x}) = \partial g(\mathbf{x}) / \partial \mathbf{x}$. Our goal is to construct a computationally efficient approximation of \mathbf{E}_j when $|\mathbf{x} - \bar{\mathbf{x}}_j| \gg l$, i.e., when evaluation point is far away from the unit cell.

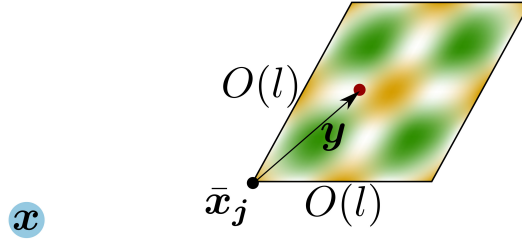


Fig. 4: Schematic of the unit cell U_j contributing to the electric field at a given point \mathbf{x} .

Towards this goal, we first consider the change of variables $\tilde{\mathbf{y}} = \mathbf{y}/l \Rightarrow d\tilde{\mathbf{y}} = d\mathbf{y}/l^3$ in 3-d. Let \tilde{U}_0 denote the rescaled unit cell. We also define the scaled charge density field $\tilde{\rho}(\tilde{\mathbf{y}})$:

$$(37) \quad \tilde{\rho}(\tilde{\mathbf{y}}) = l\rho(\bar{\mathbf{x}}_j + l\tilde{\mathbf{y}}) = l\rho(\bar{\mathbf{x}}_j + \mathbf{y})$$

for all $\tilde{\mathbf{y}} \in \tilde{U}_0$. This scaling ensures that the dipole density \mathbf{p}_j , for $\mathbf{j} \in \bar{L}$, defined as

$$(38) \quad \mathbf{p}_j = \frac{1}{|U_0|} \int_{U_0} \rho(\bar{\mathbf{x}}_j + \mathbf{y}) \mathbf{y} d\mathbf{y}$$

satisfies

$$(39) \quad \mathbf{p}_j = \frac{1}{|\tilde{U}_0|} \int_{\tilde{U}_0} \tilde{\rho}(\tilde{\mathbf{y}}) d\tilde{\mathbf{y}}.$$

That is, the dipole density is invariant under the rescaling.

Note also that the charge-neutrality condition (18) implies

$$(40) \quad \int_{\tilde{U}_0} \tilde{\rho}(\tilde{\mathbf{y}}) d\tilde{\mathbf{y}} = 0.$$

Using the rescaling $\tilde{\mathbf{y}} = \mathbf{y}/l$ in (35), we get

$$(41) \quad \mathbf{E}_j(\mathbf{x}) = -l^2 \int_{\tilde{U}_0} \tilde{\rho}(\tilde{\mathbf{y}}) \nabla g(\mathbf{x} - \bar{\mathbf{x}}_j - l\tilde{\mathbf{y}}) d\tilde{\mathbf{y}}.$$

A Taylor expansion of the integrand above gives:

$$(42) \quad \nabla g(\mathbf{x} - \bar{\mathbf{x}}_j - l\tilde{\mathbf{y}}) = \nabla g(\mathbf{x} - \bar{\mathbf{x}}_j) + \nabla^2 g(\mathbf{x} - \bar{\mathbf{x}}_j)(-l\tilde{\mathbf{y}}) + \frac{1}{2} \nabla^3 g(\mathbf{x} - \bar{\mathbf{x}}_j - l\boldsymbol{\xi})(-l\tilde{\mathbf{y}}) \otimes (-l\tilde{\mathbf{y}}),$$

where $\boldsymbol{\xi} \in \tilde{U}_0$, and $\boldsymbol{\xi}$ may depend on $\mathbf{x} - \bar{\mathbf{x}}_j$ and $\tilde{\mathbf{y}}$; such a $\boldsymbol{\xi}$ exists from the Mean-Value theorem. We combine this with (41) to get

$$(43) \quad \begin{aligned} \mathbf{E}_j(\mathbf{x}) &= -l^2 \int_{\tilde{U}_0} \tilde{\rho}(\tilde{\mathbf{y}}) \nabla g(\mathbf{x} - \bar{\mathbf{x}}_j) d\tilde{\mathbf{y}} + l^3 \int_{\tilde{U}_0} \tilde{\rho}(\tilde{\mathbf{y}}) \nabla^2 g(\mathbf{x} - \bar{\mathbf{x}}_j) \tilde{\mathbf{y}} d\tilde{\mathbf{y}} - \frac{l^4}{2} \int_{\tilde{U}_0} \tilde{\rho}(\tilde{\mathbf{y}}) \nabla^3 g(\mathbf{x} - \bar{\mathbf{x}}_j - l\boldsymbol{\xi}) \tilde{\mathbf{y}} \otimes \tilde{\mathbf{y}} d\tilde{\mathbf{y}} \\ &= |\tilde{U}_0| l^3 \nabla^2 g(\mathbf{x} - \bar{\mathbf{x}}_j) \mathbf{p}_j - \underbrace{\frac{l^4}{2} \int_{\tilde{U}_0} \tilde{\rho}(\tilde{\mathbf{y}}) \nabla^3 g(\mathbf{x} - \bar{\mathbf{x}}_j - l\boldsymbol{\xi}) \tilde{\mathbf{y}} \otimes \tilde{\mathbf{y}} d\tilde{\mathbf{y}}}_{=:\Psi_j(\mathbf{x})}, \end{aligned}$$

where we used (40) and (39) to simplify and reach the final expression. We denote the approximation of $\mathbf{E}_j(\mathbf{x})$ in terms of the dipole field by $\mathbf{E}_j^a(\mathbf{x})$, i.e.,

$$(44) \quad \mathbf{E}_j^a(\mathbf{x}) = |\tilde{U}_0| l^3 \nabla^2 g(\mathbf{x} - \bar{\mathbf{x}}_j) \mathbf{p}_j$$

so that the error is

$$(45) \quad \mathbf{E}_j(\mathbf{x}) - \mathbf{E}_j^a(\mathbf{x}) = \Psi_j(\mathbf{x}).$$

Bound on the Error. It is useful to bound the error $\Psi_j(\mathbf{x})$. Let $\mathbf{a} = \mathbf{x} - \bar{\mathbf{x}}_j$ and $\mathbf{b} = l\boldsymbol{\xi}$. Using the bound below:

$$(46) \quad |\nabla^3 g(\mathbf{x})| = \left| \nabla \left(-\frac{1}{4\pi\epsilon_0 |\mathbf{x}|^3} \left[\mathbf{I} - 3 \frac{\mathbf{x}}{|\mathbf{x}|} \otimes \frac{\mathbf{x}}{|\mathbf{x}|} \right] \right) \right| \leq \frac{12}{4\pi\epsilon_0 |\mathbf{x}|^4}$$

and the fact that $|\tilde{\mathbf{y}}| \leq \hat{c}$ and $|\boldsymbol{\xi}| \leq \hat{c}$, for $\tilde{\mathbf{y}}, \boldsymbol{\xi} \in \tilde{U}_0$ (see (7)), we have

$$(47) \quad \begin{aligned} |\nabla^3 g(\mathbf{a} - \mathbf{b}) \tilde{\mathbf{y}} \otimes \tilde{\mathbf{y}}| &\leq \hat{c}^2 |\nabla^3 g(\mathbf{a} - \mathbf{b})| \leq \underbrace{\frac{12\hat{c}^2}{4\pi\epsilon_0}}_{=:C} \frac{1}{|\mathbf{a} - \mathbf{b}|^4} = \frac{C}{|\mathbf{a}|^4} \frac{|\mathbf{a}|^4}{|\mathbf{a} - \mathbf{b}|^4} \\ &\leq \frac{C}{|\mathbf{a}|^4} \frac{|\mathbf{a}|^4}{||\mathbf{a}| - |\mathbf{b}||^4} = \frac{C}{|\mathbf{a}|^4} \left(\frac{1}{1 - \frac{|\mathbf{b}|}{|\mathbf{a}|}} \right)^4 \leq \frac{C}{|\mathbf{a}|^4} \left(\frac{1}{1 - \frac{\hat{c}l}{|\mathbf{a}|}} \right)^4 \\ &= \frac{C}{|\mathbf{a}|^4} \left(\sum_{n=0}^{\infty} \left(\frac{\hat{c}l}{|\mathbf{a}|} \right)^n \right)^4 = \frac{C}{|\mathbf{a}|^4} \sum_{n=0}^{\infty} f_n \left(\frac{\hat{c}l}{|\mathbf{a}|} \right)^n = \frac{C}{l^4} \sum_{n=0}^{\infty} f_n \hat{c}^n \left(\frac{l}{|\mathbf{a}|} \right)^{n+4}, \end{aligned}$$

where we have used the reverse triangle inequality $|\mathbf{a} - \mathbf{b}| \geq ||\mathbf{a}| - |\mathbf{b}||$; the bound on $|\mathbf{b}| \leq \hat{c}l$; the series expansion of $\frac{1}{(1-x)} = \sum_{n=0}^{\infty} x^n$; and the fact that $\left(\sum_{n=0}^{\infty} x^n \right)^4 = \sum_{n=0}^{\infty} f_n x^n$ with $f_n = \sum_{m=0}^{n-1} (n-m)(m+1)$. We use (47) in the definition of $\Psi_j(\mathbf{x})$ from (43) to find:

$$(48) \quad |\Psi_j(\mathbf{x})| \leq \frac{l^4}{2} \int_{\tilde{U}_0} \tilde{\rho}(\tilde{\mathbf{y}}) \left[\frac{C}{l^4} \sum_{n=0}^{\infty} f_n \hat{c}^n \left(\frac{l}{|\mathbf{x} - \bar{\mathbf{x}}_j|} \right)^{n+4} \right] d\tilde{\mathbf{y}} \leq |\tilde{U}_0| l^3 \left[C \sum_{n=0}^{\infty} f_n \hat{c}^n \frac{l^{n+1}}{|\mathbf{x} - \bar{\mathbf{x}}_j|^{n+4}} \right],$$

where we have redefined the constant C as

$$(49) \quad C = \left(\frac{12\hat{c}^2}{4\pi\epsilon_0} \right) \frac{\int_{\tilde{U}_0} |\tilde{\rho}(\tilde{\mathbf{y}})| d\tilde{\mathbf{y}}}{2|\tilde{U}_0|}.$$

All terms in (43) beyond the dipole correspond to the higher-order multipoles that could be explicitly included in the calculation to improve the accuracy; the FMM does exactly that, and the error is controlled by including higher order multipole terms as necessary. In FMM, the number of terms that are included depends on the distance between the cluster of charges and the evaluation point, $|\mathbf{x} - \bar{\mathbf{x}}_j|$, and the required tolerance. In our approach, we use only the dipole term, so $\mathbf{E}_j(\mathbf{x}) \approx \mathbf{E}_j^a(\mathbf{x})$, and ignore all the higher order terms collected in $\Psi_j(\mathbf{x})$; a bound on the error $\Psi_j(\mathbf{x})$ as a function of distance $|\mathbf{x} - \bar{\mathbf{x}}_j|$ and lattice size l is obtained (48). As the distance $|\mathbf{x} - \bar{\mathbf{x}}_j|$ decreases, i.e., the unit cell gets closer to the evaluation point, the error will increase. Thus, we only use this approximation at sufficiently large distances such that the bound on the error is below our tolerance. The contributions to the electric field from the unit cells that are close to the point of evaluation are calculated exactly using (34). Following this line of thought, we next derive an approximation of the electric field from all the unit cells in lattice \bar{L} , and obtain a bound on the total error due to the approximation. The bound on the error will be used to determine where – i.e., how far from the evaluation point \mathbf{x} – the approximation of the electric field can be used while keeping the error within a specified tolerance.

4.2. Contribution from all unit cells in the body. First, we divide the electric field at a point \mathbf{x} into two contributions: one from the unit cells in the atomistic region, and the other from unit cells in the coarse-grained region:

$$(50) \quad \mathbf{E}(\mathbf{x}) = \sum_{j \in \bar{L}^{at}} \mathbf{E}_j(\mathbf{x}) + \sum_{j \in \bar{L}^{co}} \mathbf{E}_j(\mathbf{x}).$$

Since the atomistic region may contain defects and involve rapidly-varying deformations, we consider the exact contribution to the electric field from all charges in this region. In the coarse-grained region, we use the first-order approximation of electric field using the dipole contribution, i.e., we replace $\mathbf{E}_j(\mathbf{x})$ by $\mathbf{E}_j^a(\mathbf{x})$, see (44). However, to control the error, we use this approximation only when the unit cells are sufficiently far away from the evaluation point \mathbf{x} , and consider the exact contributions from cells that are near the point \mathbf{x} .

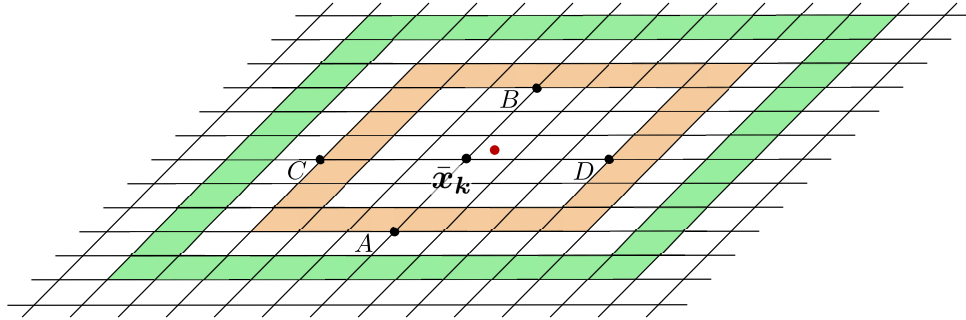


Fig. 5: Example of shells in a 2-d lattice. Here, the red dot is the evaluation point \mathbf{x} and the nearby black dots are the lattice sites $\mathbf{k} = (k_1, k_2)$ such that $\mathbf{x} \in U_{\mathbf{k}}$. The orange unit cells form the shell $\Omega^{sh}(\mathbf{x}, 2)$ (for $p = 2$); the lattice sites A, B, C, D correspond to indices $\{(k_1, k_2 - 3), (k_1, k_2 + 3), (k_1 - 3, k_2), (k_1 + 3, k_2)\} \subset A^{sh}(\mathbf{x}, 2)$, respectively. The green unit cells similarly form the shell $\Omega^{sh}(\mathbf{x}, 4)$, i.e., $\Omega^{sh}(\mathbf{x}, p)$ for $p = 4$.

To describe the proposed approximation framework, we first introduce the partitioning of Ω^{co} into shells; see Figure 5. Fix \mathbf{x} , and let $\mathbf{k} = \mathbf{k}(\mathbf{x}) \in \bar{L}$ is such that $\mathbf{x} \in U_{\mathbf{k}}$. Given an integer $p \geq 0$, we define the integer tuple set $A^{sh}(\mathbf{x}, p)$ as follows

$$(51) \quad A^{sh}(\mathbf{x}, p) = \bar{A}(\mathbf{x}, p) - \bar{A}(\mathbf{x}, p - 1),$$

where

$$(52) \quad \bar{A}(\mathbf{x}, p) = \begin{cases} \bar{L}^{co} \cap ([k_1 - p, k_1 + p] \times [k_2 - p, k_2 + p] \times [k_3 - p, k_3 + p]), & \text{if } p \geq 0, \\ \emptyset, & \text{if } p < 0 \end{cases}$$

with $\mathbf{k} = \mathbf{k}(\mathbf{x}) = (k_1, k_2, k_3) \in \bar{L}$ such that $\mathbf{x} \in U_{\mathbf{k}}$. We use the notation $[k_1 - p, k_1 + p] \times [k_2 - p, k_2 + p] \times [k_3 - p, k_3 + p]$ to denote the Cartesian product of three sets. The set $A^{sh}(\mathbf{x}, p)$ consists of unit cells within $p + 1$ integer distance of unit cell \mathbf{k} ; however, all cells within p integer distance of lattice \mathbf{k} are removed. Then, the set $A_p^{sh}(\mathbf{x})$ gives us the shell $\Omega^{sh}(\mathbf{x}, p)$ formed by unit cells $\{U_j\}_{j \in A^{sh}(\mathbf{x}, p)}$:

$$(53) \quad \Omega^{sh}(\mathbf{x}, p) = \bigcup_{i \in A^{sh}(\mathbf{x}, p)} U_i.$$

It is easy to see that the union of shells $\{\Omega^{sh}(\mathbf{x}, p)\}_{p \in \mathbb{N}}$ gives the covering of domain Ω^{co} . Figure 5 shows the shell region corresponding to the evaluation point \mathbf{x} .

We fix an integer p_0 such that for all shells, $\{A^{sh}(\mathbf{x}, i)\}_{i=0}^{p_0}$, we compute the electric field exactly, and for all the remaining unit cells in Ω^{co} , the approximation E_j^a is used. We collect all the unit cells for which we use the exact electric field in the set $A^{sh,ex}(\mathbf{x}, p_0)$ as follows

$$(54) \quad A^{sh,ex}(\mathbf{x}, p_0) := \bigcup_{i=0}^{p_0} A^{sh}(\mathbf{x}, i) \subset \bar{L}^{co}$$

and the domain associated with the unit cells in $A^{sh,ex}(\mathbf{x}, p_0)$ is defined as

$$(55) \quad \Omega^{sh,ex}(\mathbf{x}, p_0) = \bigcup_{j \in A^{sh,ex}(\mathbf{x}, p_0)} U_j.$$

In summary, the approximation takes the form

$$(56) \quad \begin{aligned} \sum_{j \in \bar{L}^{co}} E_j(\mathbf{x}) &= \sum_{p=0}^{\infty} \left(\sum_{j \in A^{sh}(\mathbf{x}, p)} E_j(\mathbf{x}) \right) = \sum_{p=0}^{p_0} \left(\sum_{j \in A^{sh}(\mathbf{x}, p)} E_j(\mathbf{x}) \right) + \sum_{p=p_0+1}^{\infty} \left(\sum_{j \in A^{sh}(\mathbf{x}, p)} E_j(\mathbf{x}) \right) \\ &\approx \sum_{p=0}^{p_0} \left(\sum_{j \in A^{sh}(\mathbf{x}, p)} E_j(\mathbf{x}) \right) + \sum_{p=p_0+1}^{\infty} \left(\sum_{j \in A^{sh}(\mathbf{x}, p)} E_j^a(\mathbf{x}) \right), \end{aligned}$$

where the approximation $E_j^a(\mathbf{x})$ of $E_j(\mathbf{x})$ has been introduced. Then, from (56) and using the definition of $A^{sh,ex}(\mathbf{x}, p_0)$, we have

$$(57) \quad \begin{aligned} \sum_{j \in \bar{L}^{co}} E_j(\mathbf{x}) &\approx \sum_{j \in A^{sh,ex}(\mathbf{x}, p_0)} E_j(\mathbf{x}) + \sum_{j \in \bar{L}^{co} - A^{sh,ex}(\mathbf{x}, p_0)} E_j^a(\mathbf{x}) \\ &= \sum_{j \in A^{sh,ex}(\mathbf{x}, p_0)} E_j(\mathbf{x}) + \sum_{j \in \bar{L}^{co} - A^{sh,ex}(\mathbf{x}, p_0)} \left[|\tilde{U}_0| l^3 \nabla^2 g(\mathbf{x} - \bar{\mathbf{x}}_j) p_j \right]. \end{aligned}$$

Next, assuming that $\bar{L}^{co} - A^{sh,ex}(\mathbf{x}, p_0)$ consists of a large number of lattice sites and using the fact that $|\tilde{U}_0| l^3$ is the

volume of the unit cell U_j , we can approximate the second term in the equation above by an integral as follows

$$\begin{aligned}
 \sum_{j \in \bar{L}^{co}} \mathbf{E}_j(\mathbf{x}) &\approx \sum_{j \in A^{sh,ex}(\mathbf{x}, p_0)} \mathbf{E}_j(\mathbf{x}) + \sum_{j \in \bar{L}^{co} - A^{sh,ex}(\mathbf{x}, p_0)} \left[\int_{U_j} \nabla^2 g(\mathbf{x} - \mathbf{z}) \mathbf{p}(\mathbf{z}) \, d\mathbf{z} \right] \\
 &= \sum_{j \in A^{sh,ex}(\mathbf{x}, p_0)} \mathbf{E}_j(\mathbf{x}) + \int_{\Omega^{co} - \Omega^{sh,ex}(\mathbf{x}, p_0)} \nabla^2 g(\mathbf{x} - \mathbf{z}) \mathbf{p}(\mathbf{z}) \, d\mathbf{z} \\
 (58) \quad &= \sum_{j \in A^{sh,ex}(\mathbf{x}, p_0)} \mathbf{E}_j(\mathbf{x}) + \int_{\partial(\Omega^{co} - \Omega^{sh,ex}(\mathbf{x}, p_0))} (\mathbf{p}(\mathbf{z}) \cdot \mathbf{n}) \nabla g(\mathbf{x} - \mathbf{z}) \, dS(\mathbf{z}) \\
 &\quad - \int_{\Omega^{co} - \Omega^{sh,ex}(\mathbf{x}, p_0)} (\nabla \cdot \mathbf{p}(\mathbf{z})) \nabla g(\mathbf{x} - \mathbf{z}) \, d\mathbf{z},
 \end{aligned}$$

where $\mathbf{p}: \Omega \rightarrow \mathbb{R}^3$ is the dipole density field that is obtained as a piecewise constant extension of the discrete dipole densities $\{\mathbf{p}_j\}_{j \in L}$. In the last expression above, we used the Gauss divergence theorem. Here, $\partial(\Omega^{co} - \Omega_{p_0}^{sh,ex}(\mathbf{x}))$ denotes the boundary of $\Omega^{co} - \Omega_{p_0}^{sh,ex}(\mathbf{x})$, \mathbf{n} the outward unit normal, and $dS(\mathbf{z})$ the area measure. Substituting (58) in (50), writing $\mathbf{E}_j(\mathbf{x})$ explicitly, and referring to the approximation of $\mathbf{E}(\mathbf{x})$ by $\mathbf{E}^a(\mathbf{x})$, we get

$$\begin{aligned}
 \mathbf{E}^a(\mathbf{x}) &= \underbrace{\sum_{j \in A^{sh,ex}(\mathbf{x}, p_0) \cup \bar{L}^{at}} \left[\sum_{\beta \in \mathbb{N}_M, \mathbf{x}_{(j,\beta)} \neq \mathbf{x}} \frac{\hat{q}_\beta}{4\pi\epsilon_0} \frac{\mathbf{x} - \bar{\mathbf{x}}_j - \mathbf{y}_\beta}{|\mathbf{x} - \bar{\mathbf{x}}_j - \mathbf{y}_\beta|^3} \right]}_{\text{exact}} \\
 (59) \quad &+ \underbrace{\int_{\partial(\Omega^{co} - \Omega^{sh,ex}(\mathbf{x}, p_0))} (\mathbf{p}(\mathbf{z}) \cdot \mathbf{n}) \nabla g(\mathbf{x} - \mathbf{z}) \, dS(\mathbf{z}) - \int_{\Omega^{co} - \Omega^{sh,ex}(\mathbf{x}, p_0)} (\nabla \cdot \mathbf{p}(\mathbf{z})) \nabla g(\mathbf{x} - \mathbf{z}) \, d\mathbf{z}}_{\text{approximate}}.
 \end{aligned}$$

The error $\mathbf{E}(\mathbf{x}) - \mathbf{E}^a(\mathbf{x})$ is only from the unit cells in $\bar{L}^{co} - A^{sh,ex}(\mathbf{x}, p_0)$ and it is given by

$$\begin{aligned}
 \mathbf{E}(\mathbf{x}) - \mathbf{E}^a(\mathbf{x}) &= \sum_{j \in \bar{L}^{co} - A^{sh,ex}(\mathbf{x}, p_0)} (\mathbf{E}_j(\mathbf{x}) - \mathbf{E}_j^a(\mathbf{x})) = \sum_{p=p_0+1}^{\infty} \left(\sum_{j \in A^{sh}(\mathbf{x}, p)} (\mathbf{E}_j(\mathbf{x}) - \mathbf{E}_j^a(\mathbf{x})) \right) \\
 (60) \quad &= \sum_{p=p_0+1}^{\infty} \left(\sum_{j \in A^{sh}(\mathbf{x}, p)} \Psi_j(\mathbf{x}) \right),
 \end{aligned}$$

where $\Psi_j(\mathbf{x})$ is defined in (43).

Bound on the error. We now compute the bound on the error $|\mathbf{E}(\mathbf{x}) - \mathbf{E}^a(\mathbf{x})|$. We analyze the error in the limit that the lattice size l goes to zero relative to the size of the body and in the limit $p_0 \rightarrow \infty$. Using (48) in (60), we have

$$\begin{aligned}
 |\mathbf{E}(\mathbf{x}) - \mathbf{E}^a(\mathbf{x})| &\leq \sum_{p=p_0+1}^{\infty} \left[\sum_{j \in A^{sh}(\mathbf{x}, p)} |\Psi_j(\mathbf{x})| \right] \\
 (61) \quad &\leq \sum_{p=p_0+1}^{\infty} \left[\sum_{j \in A^{sh}(\mathbf{x}, p)} |\tilde{U}_0| l^3 \left(C \sum_{n=0}^{\infty} f_n \hat{c}^n \frac{l^{n+1}}{|\mathbf{x} - \bar{\mathbf{x}}_j|^{n+4}} \right) \right] \\
 &\approx \sum_{p=p_0+1}^{\infty} \left[\sum_{j \in A^{sh}(\mathbf{x}, p)} \int_{U_j} \left(C \sum_{n=0}^{\infty} f_n \hat{c}^n \frac{l^{n+1}}{|\mathbf{x} - \mathbf{z}|^{n+4}} \right) d\mathbf{z} \right],
 \end{aligned}$$

where in the last line we approximated the sum by an integral over U_j . We note that in the limit of $l \rightarrow 0$, all error terms go exactly to zero. The approximation becomes exact in the limit, as expected from [10, 26]. We also note that as $|\mathbf{x} - \mathbf{z}|$ gets larger, the relative error in (61) decreases. To demonstrate this relationship, we further analyze the upper bound in (61) as follows. For fixed p , note that for $\mathbf{z} \in U_j, \mathbf{j} \in A^{sh}(\mathbf{x}, p)$ – see (51) for the definition of $A^{sh}(\mathbf{x}, p)$ – we have:

$$(62) \quad (p-1)l \leq |\mathbf{x} - \mathbf{z}| \leq \hat{c}pl,$$

where we used (7). Further, it can be shown that

$$(63) \quad \sum_{\mathbf{j} \in A^{sh}(\mathbf{x}, p)} \int_{U_j} \left(C \sum_{n=0}^{\infty} f_n \hat{c}^n \frac{l^{n+1}}{|\mathbf{x} - \mathbf{z}|^{n+4}} \right) d\mathbf{z} \leq \left(C \sum_{n=0}^{\infty} f_n \hat{c}^n \frac{l^{n+1}}{((p-1)l)^{n+4}} \right) \sum_{\mathbf{j} \in A^{sh}(\mathbf{x}, p)} \int_{U_j} d\mathbf{z} \\ = \left(C \sum_{n=0}^{\infty} f_n \hat{c}^n \frac{l^{n+1}}{((p-1)l)^{n+4}} \right) |U_0| |A^{sh}(\mathbf{x}, p)|,$$

where $|U_0| = l^3 |\tilde{U}_0|$, $|\tilde{U}_0| = O(1)$, and $|A^{sh}(\mathbf{x}, p)|$ is the number of elements in the set. Based on the definition of $A^{sh}(\mathbf{x}, p)$ in (51), we have, for $p \geq 0$,

$$(64) \quad |A^{sh}(\mathbf{x}, p)| = |\bar{A}(\mathbf{x}, p)| - |\bar{A}(\mathbf{x}, p-1)| \leq (2p+1)^3 - (2(p-1)+1)^3 = 2(1+12p^2).$$

Also, suppose p_{max} is the smallest integer such that $A^{sh}(\mathbf{x}, p_{max})$ is empty; then, combining (61), (63), and (64), we have that:

$$(65) \quad |\mathbf{E}(\mathbf{x}) - \mathbf{E}^a(\mathbf{x})| \leq \sum_{p=p_0+1}^{p_{max}} \left[\left(C \sum_{n=0}^{\infty} f_n \hat{c}^n \frac{l^{n+1}}{((p-1)l)^{n+4}} \right) l^3 |\tilde{U}_0| 2(1+12p^2) \right] \\ = C \sum_{p=p_0+1}^{p_{max}} \left[\sum_{n=0}^{\infty} f_n \hat{c}^n \frac{2(1+12p^2)}{(p-1)^{n+4}} \right] \\ \leq C \sum_{p=p_0+1}^{\infty} \left[\sum_{n=0}^{\infty} f_n \hat{c}^n \frac{2(1+12p^2)}{(p-1)^{n+4}} \right],$$

where we have redefined the constant C as follows

$$(66) \quad C = \left(\frac{12\hat{c}^2}{4\pi\epsilon_0} \right) \frac{\int_{\tilde{U}_0} |\tilde{\rho}(\tilde{\mathbf{y}})| d\tilde{\mathbf{y}}}{2|\tilde{U}_0|} |\tilde{U}_0| = \left(\frac{12\hat{c}^2}{4\pi\epsilon_0} \right) \frac{\int_{\tilde{U}_0} |\tilde{\rho}(\tilde{\mathbf{y}})| d\tilde{\mathbf{y}}}{2}.$$

In (65), if we take the limit of $p_0 \rightarrow \infty$, we obtain again the result that the error is identically zero, as was the case in the limit of $l \rightarrow 0$. Physically, these are equivalent: one corresponds to shrinking the unit cell size and the other to increasing the distance $|\mathbf{x} - \bar{\mathbf{x}}_j|$ between the lattice site location and the evaluation point.

In summary, we use the exact contribution to the electric field from the shells $\Omega^{sh,ex}(\mathbf{x}, p_0) = \{\Omega^{sh}(\mathbf{x}, p)\}_{p=p_0}^{p_0}$ and the atomistic region Ω^{at} , and use the approximation for the remaining contributions. That is:

$$(67) \quad \mathbf{E}^a(\mathbf{x}) = \underbrace{\sum_{\mathbf{j} \in A^{sh,ex}(\mathbf{x}, p_0) \cup \bar{L}^{at}} \left[\sum_{\beta \in \mathbb{N}_M, \mathbf{x}_{(j,\beta)} \neq \mathbf{x}} \frac{\hat{q}_\beta}{4\pi\epsilon_0} \frac{\mathbf{x} - \bar{\mathbf{x}}_j - \mathbf{y}_\beta}{|\mathbf{x} - \bar{\mathbf{x}}_j - \mathbf{y}_\beta|^3} \right]}_{\text{exact}} \\ + \underbrace{\int_{\partial(\Omega^{co} - \Omega^{sh,ex}(\mathbf{x}, p_0))} (\mathbf{p}(\mathbf{z}) \cdot \mathbf{n}) \nabla g(\mathbf{x} - \mathbf{z}) dS(\mathbf{z}) - \int_{\Omega^{co} - \Omega^{sh,ex}(\mathbf{x}, p_0)} (\nabla \cdot \mathbf{p}(\mathbf{z})) \nabla g(\mathbf{x} - \mathbf{z}) d\mathbf{z}}_{\text{approximate}}.$$

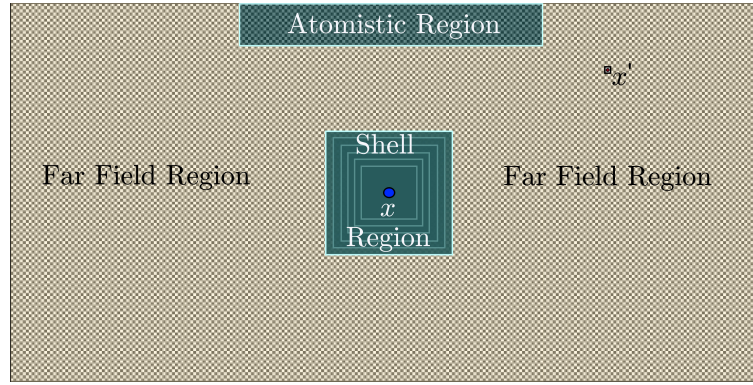


Fig. 6: Partition of the domain into the atomistic and the coarse-grained (far field) region. Further, the coarse-grained region is divided into two parts: the shell region and the region outside the outer shell. A single unit cell located at x' in the far field region is also shown.

The three different regions from which the contributions to the electric field are computed are shown in Figure 6. The integer p_0 associated with the outer shell beyond which the electric field is approximated is selected to control the error given by

$$(68) \quad |\mathbf{E}(\mathbf{x}) - \mathbf{E}^a(\mathbf{x})| \leq C \sum_{p=p_0+1}^{p_{max}} \left[\sum_{n=0}^{\infty} f_n \hat{c}^n \frac{2(1+12p^2)}{(p-1)^{n+4}} \right] \leq C \sum_{p=p_0+1}^{\infty} \left[\sum_{n=0}^{\infty} f_n \hat{c}^n \frac{2(1+12p^2)}{(p-1)^{n+4}} \right].$$

In section 6, we will evaluate the error both in closed-form and numerically using GaN as a test material for a variety of different p_0 shell region sizes.

5. Numerical Implementation. Our implementation of the QC method combining the short-range and long-range electrostatic interactions for a multilattice system is based on the version of the QC code described in [19]. We start by providing a brief overview of the QC code and then describe the implementation of the approximation of the electrostatic interactions developed in the previous section.

The original QC code is a mix of C, C++, and Fortran, with a majority of the code written in C. The code takes lattices as an input and meshes each lattice separately as discussed in Section 3. Data structures including hash tables and neighbor lists (for interatomic short-range interactions) are used to store the required information for calculating forces on atoms. A variety of mechanical loads can be applied, and the code solves the static equilibrium problem (31) under external loading.

We implement electrostatic interactions following Section 4 in the QC code by creating a C++ singleton class that handles all electrostatic calculations. The key calculation carried out in the singleton class is to compute the electric fields at the rep. and cluster atoms (i.e., the atoms in the neighborhood of the rep. atoms); once the electric field is computed, the force on any atom due to the electrostatic interactions can be obtained by multiplying the electric field at the atom and the charge carried by the atom. The base QC code interfaces with the singleton class and calls the method of the class to update the electric fields whenever the configuration has changed. The method computes the electric field in three steps which we discuss next.

The first step is to account for the exact contribution from the unit cells in the shells $\Omega^{sh,ex}(\mathbf{x}, p_0) = \{\Omega^{sh}(\mathbf{x}, p)\}_{p=0}^{p_0}$ and the atomistic region Ω^{at} , see (67). We use hash tables keyed by the triple integer of lattice site coordinates unique to each atom to store lists of atoms in Ω^{at} and shells $\Omega^{sh,ex}(\mathbf{x}, p_0)$ for a given rep. atom \mathbf{x} for a quicker evaluation. The size of the shell region, i.e., the integer p_0 , is controlled via an input integer.

The second step is to include all approximate contributions to the electric field from $\Omega^{co} - \Omega^{sh,ex}(\mathbf{x}, p_0)$. The discrete polarization densities $\{\mathbf{p}_j\}_{j \in L}$ are updated using (38). We then use the polarization density field – defined

as a piecewise constant extension of discrete polarization densities – to calculate the electric field; see the second part of (67). For simplicity, we assume that the polarization density is constant in every finite element and the polarization density of an element is computed at a unit cell closest to the center of an element. Due to this simplification, the integral over $\Omega^{co} - \Omega^{sh,ex}(\mathbf{x}, p_0)$, see (67), is equivalent to calculating the jump in the polarization, $[\![\mathbf{p}_2 - \mathbf{p}_1]\!] \cdot \mathbf{n} = \sigma$, between finite elements along the edges / faces. The remaining contribution from the boundary $\partial(\Omega^{co} - \Omega^{sh,ex}(\mathbf{x}, p_0))$ can be computed easily using $\mathbf{p} \cdot \mathbf{n}$. The boundary $\partial(\Omega^{co} - \Omega^{sh,ex}(\mathbf{x}, p_0))$ includes parts of the exterior boundary, i.e., parts of $\partial\Omega$, and the interior boundary. The conditions on the exterior boundaries are simply controlled with input options of a free surface boundary, a charge-neutralized (infinite domain) boundary, or a specified charge density on the boundary. The contributions to the electric field from $[\![\mathbf{p}_2 - \mathbf{p}_1]\!] \cdot \mathbf{n} = \sigma$ and the exterior boundaries are computed using (67) with an adaptive numerical integration scheme.

The contribution to the electric field from the interior boundary of Ω^{co} at the intersection of Ω^{co} and $\Omega^{sh,ex}(\mathbf{x}, p_0)$ requires additional work, see (67). We note that the outer surface of $\Omega^{sh,ex}(\mathbf{x}, p_0)$ is trapezoidal, see Figure 5. Thus, to compute the contribution from the interior part of $\partial(\Omega^{co} - \Omega^{sh,ex}(\mathbf{x}, p_0))$, we need to compute the intersection of a trapezoidal (associated with the outer boundary of $\Omega^{sh,ex}(\mathbf{x}, p_0)$) with a triangulated mesh. A contribution of $\mathbf{p} \cdot \mathbf{n}$ to the electric field then occurs on this intersection, where the polarization comes from the intersected elements. The intersection of the trapezoidal with a triangulated mesh is computed using the computational geometric library CGAL [47]. Once we have the list of intersecting planes, we compute the integral in (67) using an adaptive numerical integration scheme.

The final step is to calculate the contribution to the electric field from the external loading which can be of different types: e.g., an applied field on the body, or a fixed charge distribution. In the case of an applied field, the appropriate terms are directly superposed on the electric field. The contributions to the electric field due to external point charges near a surface are added exactly using the electrostatic interaction kernel.

We note that the above steps must be carried out for every rep. atom in Ω . The electric field at a ghost atom \mathbf{x}_I can be computed by interpolating the electric field at the rep. atoms, i.e.,

$$\mathbf{E}(\mathbf{x}_I) = \sum_{J \in L^r} \mathcal{N}_J(\mathbf{X}_I) \mathbf{E}(\mathbf{x}_J).$$

We assume that the interpolation of the electric field does not introduce significant errors. Since the ghost atoms only exist in the coarse-grained region Ω^{co} , and it is assumed that in Ω^{co} the deformation is slowly varying, the error due to the approximation of the electric field at the ghost atoms using interpolation is expected to be small. With the electric field calculated, the base QC code requests the electric field at all required atoms and calculates the force by multiplying the field with the charge on the atom. This force is then added to the short-range forces calculated in the base QC code to obtain the total internal force. Finally, the conjugate-gradient method is used to minimize the energy (31).

All electrostatic calculation in the code are implemented with threading for high performance computing. We use a queue structure for each thread to grab additional chunks of work. There are multiple potential optimizations for the future in terms of trade-offs between work chunk size, the number of threads, and the underlying data structures sizes. The optimal parameterization will depend on material properties, system geometry, and computational hardware, among other factors.

6. Results. To demonstrate the effectiveness of the proposed method, we consider a wurtzite crystal Gallium Nitride (GaN) that has four atoms per unit cell: two Gallium (Ga) and two Nitrogen (N) atoms. We assume a crystal structure parameterization using a GaN core-shell potential [48]. We study the convergence of the electrostatic approximation as the integer p_0 is increased; p_0 is such that the electric field from unit cells outside the shell $\Omega^{sh}(\mathbf{x}, p_0)$ are approximated using the dipole term. GaN is a III-IV type semiconductor with a polarization in the 0001 direction [49]. The effective charges are +2 for Ga, -2.5 for the N (electron) shell, and 0.5 for the N core. All of the following results assume charge neutralized boundary conditions; thus the size of the simulation does not matter, only the size of the exact summation region.

We start by computing the formal error bound from (68). The constant C is calculated for the GaN wurtzite structure. We calculate the total error in the electric field at a single evaluation point assuming an infinite crystal surrounding it. The total error converges (Figure 7) to a limiting value as expected from the convergence properties of

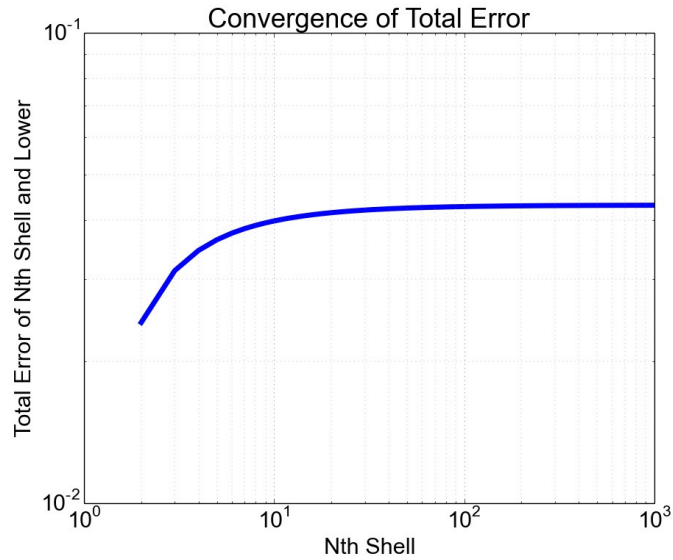


Fig. 7: The convergence of the bound on the total error in the electric field from (68) for an infinite crystal. Each successive shell adds less total error as expected because of the increased distance from evaluation point.

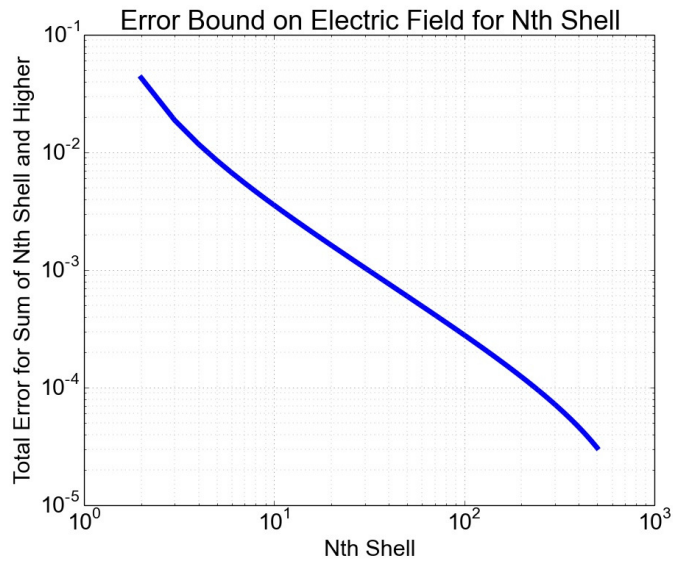


Fig. 8: The error bound for the electric field with an exact atomistic summation performed with N unit cells.

(68). We also calculate the error bound if a calculation is performed exactly within the first N shells of unit cells; as N increases, the error is expected to get smaller and smaller, as observed in Figure 8. Hence, if 10^{-3} is an acceptable error for approximation of the electric field, the contributions to the electric field from unit cells within the first 13 shells surrounding the evaluation point must be exact. The contribution to the electric field from the rest of Ω can be approximated using the dipole term.

We next calculate the error in the electric field from the computational implementation in the QC code. GaN in

Charge Density on Interior Boundary

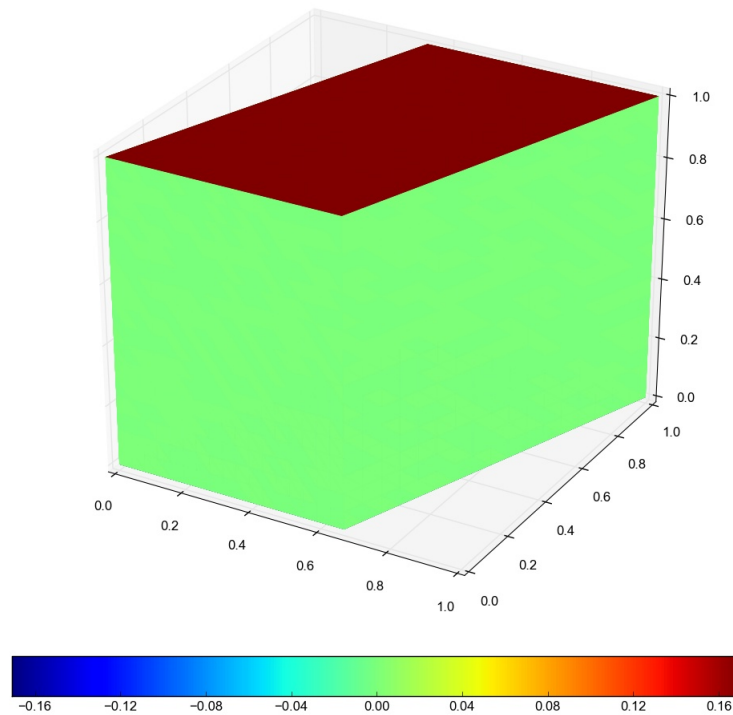


Fig. 9: The charge density on the top (0001-plane) of the interior trapezoidal boundary between the exact atomistic region and the approximated region. The size of the exact atomistic region is 8 shells of trapezoidal unit cells.

the wurtzite configuration only has polarization in the 0001-direction, so the interior boundary with the exact atomistic region will only have a charge distribution on the 0001 faces of the trapezoidal shell. Figure 9 shows the charge density from the interior boundary of the exact atomistic region and the approximated region centered about an evaluation point \mathbf{x} . Figure 10 shows the contribution to the electric field in the 0001-direction from the same interior boundary. Figure 11 shows the convergence of the electric field calculations for a single evaluation point. The three line plots show the different levels of adaptive quadrature used to solve (67). The resulting convergence is well below the error bound from Figure 8 and decreases as expected.

7. Concluding Remarks. We have developed a method to account for electrostatic interactions in the Quasicontinuum (QC) method in the setting of general geometries. Our method is inspired by elements of the Fast Multiple Method – in that we adaptively use exact and coarse-grained approximations – and the Reaction Field Method – in that we use a coarse-grained continuum approximation outside a defect region of interest. However, we go beyond these methods in the context of a crystal with defects by exploiting homogenization results to obtain efficient coarse-graining schemes with error control, and do not make any assumptions on the nature of the continuum approximation.

We implement and demonstrate the method in a high-performance parallel computing framework and within an existing QC implementation. The numerical calculations show the efficiency of the method and the accuracy of the method in terms of satisfying the rigorous error bounds. The error bounds provide the ability to transparently balance between the computational cost, numerical error, method error, problem size, error tolerance, and computational hardware.

Contribution to Electric Field from Interior Boundary

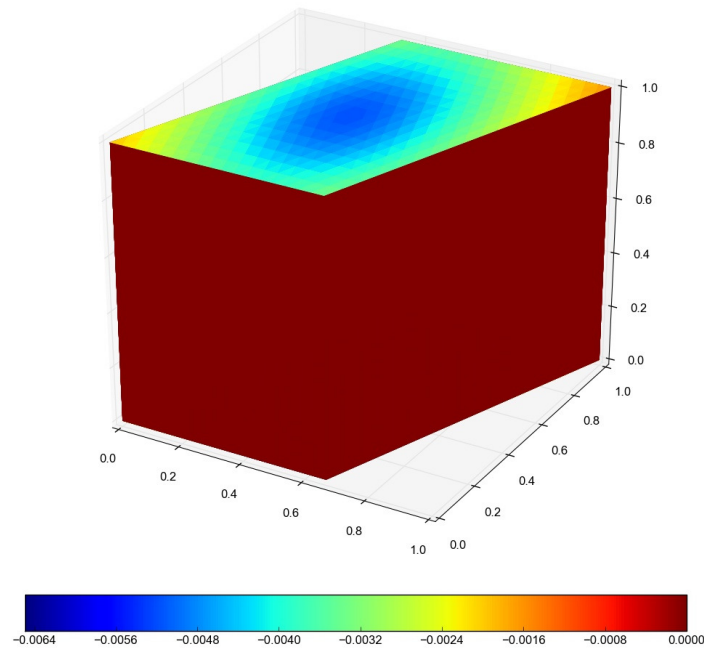


Fig. 10: The contribution to the electric field in the 0001-direction from the top (0001-plane) of the interior trapezoidal boundary between the exact atomistic region and the approximated region. The size of the exact atomistic region is 8 shells of trapezoidal unit cells.

Acknowledgements. We thank the National Science Foundation for support through XSEDE resources provided by the Pittsburgh Supercomputing Center. This paper draws from the doctoral dissertations of Prashant K. Jha and Jason Marshall at Carnegie Mellon University [50, 14]. We acknowledge financial support from ARO (W911NF-17-1-0084, MURI W911NF-19-1-0245), ONR (N00014-18-1-2528), AFOSR (MURI FA9550-18-1-0095), NSF (1921857), and the ARL Journeyman Fellowship.

REFERENCES

- [1] Grasinger, M., and Dayal, K., 2020. "Statistical mechanical analysis of the electromechanical coupling in an electrically-responsive polymer chain". *Soft Matter*, **16**(27), pp. 6265–6284.
- [2] Grasinger, M., and Dayal, K., 2021. "Architected elastomer networks for optimal electromechanical response". *Journal of the Mechanics and Physics of Solids*, **146**, p. 104171.
- [3] Grasinger, M., Mozaffari, K., and Sharma, P., 2021. "Flexoelectricity in soft elastomers and the molecular mechanisms underpinning the design and emergence of giant flexoelectricity". *Proceedings of the National Academy of Sciences*, **118**(21), p. e2102477118.
- [4] Grasinger, M., Dayal, K., deBotton, G., and Purohit, P. K., 2022. "Statistical mechanics of a dielectric polymer chain in the force ensemble". *Journal of the Mechanics and Physics of Solids*, **158**, p. 104658.
- [5] Torbati, M., Mozaffari, K., Liu, L., and Sharma, P., 2022. "Coupling of mechanical deformation and electromagnetic fields in biological cells". *Reviews of Modern Physics*, **94**(2), p. 025003.
- [6] Liu, L., and Sharma, P., 2018. "Emergent electromechanical coupling of electrets and some exact relations—the effective properties of soft materials with embedded external charges and dipoles". *Journal of the Mechanics and Physics of Solids*, **112**, pp. 1–24.
- [7] Chen, L., Yang, X., Wang, B., Yang, S., Dayal, K., and Sharma, P., 2021. "The interplay between symmetry-breaking and symmetry-preserving bifurcations in soft dielectric films and the emergence of giant electro-actuation". *Extreme Mechanics Letters*, **43**, p. 101151.
- [8] Ahmadpoor, F., Deng, Q., Liu, L., and Sharma, P., 2013. "Apparent flexoelectricity in lipid bilayer membranes due to external charge and dipolar distributions". *Physical Review E*, **88**(5), p. 050701.

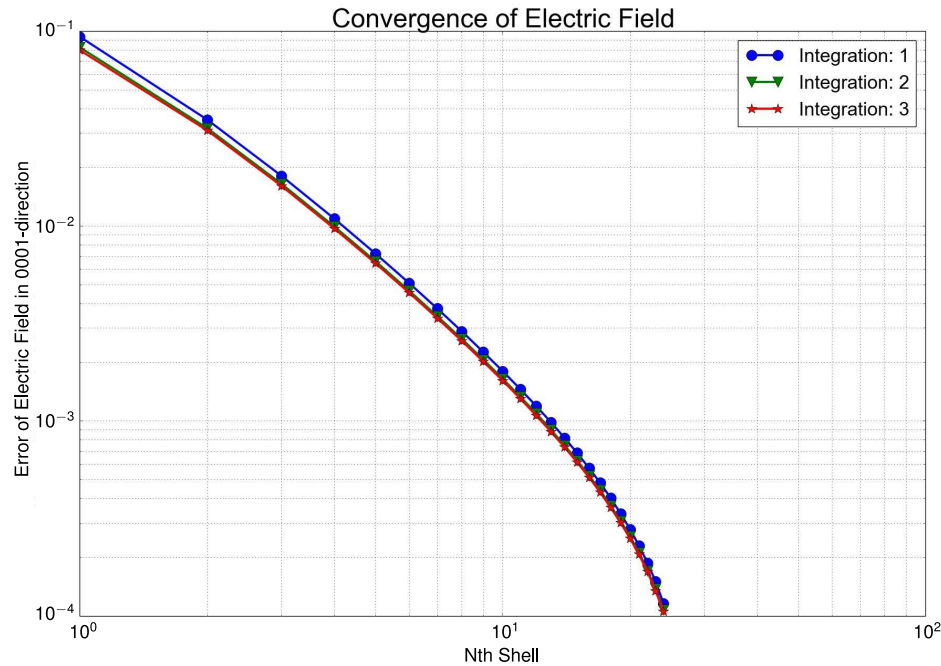


Fig. 11: Numerical convergence of the electric field in the 0001-direction from the QC code of an infinite single crystal of wurtzite GaN. The integration labels denote an increasing number of numerical quadrature points.

- [9] Liu, L., and Sharma, P., 2013. "Flexoelectricity and thermal fluctuations of lipid bilayer membranes: Renormalization of flexoelectric, dielectric, and elastic properties". *Physical Review E*, **87**(3), p. 032715.
- [10] James, R. D., and Müller, S., 1994. "Internal variables and fine-scale oscillations in micromagnetics". *Continuum Mechanics and Thermodynamics*, **6**, pp. 291–336. 10.1007/BF01140633.
- [11] Sharp, K. A., 1994. "Electrostatic interactions in macromolecules". *Current Opinion in Structural Biology*, **4**(2), pp. 234–239.
- [12] Xiao, Y., 2005. "The influence of oxygen vacancies on domain patterns in ferroelectric perovskites". PhD thesis, California Institute of Technology.
- [13] Steigmann, D. J., 2018. "Mechanics and physics of lipid bilayers". In *The role of mechanics in the study of lipid bilayers*. Springer, pp. 1–61.
- [14] Marshall, J., 2014. "Atomistic multiscale modeling with long-range electrostatic interactions". PhD thesis, Carnegie Mellon University.
- [15] Tadmor, E., and Miller, R., 2005. "The theory and implementation of the quasicontinuum method". In *Handbook of Materials Modeling*. Springer, pp. 663–682.
- [16] Miller, R. E., and Tadmor, E., 2009. "A unified framework and performance benchmark of fourteen multiscale atomistic/continuum coupling methods". *Modelling and Simulation in Materials Science and Engineering*, **17**(5), p. 053001.
- [17] Tadmor, E. B., and Miller, R. E., 2011. *Modeling materials: continuum, atomistic and multiscale techniques*. Cambridge University Press.
- [18] Kulkarni, Y., Knap, J., and Ortiz, M., 2008. "A variational approach to coarse graining of equilibrium and non-equilibrium atomistic description at finite temperature". *Journal of the Mechanics and Physics of Solids*, **56**(4), pp. 1417–1449.
- [19] Knap, J., and Ortiz, M., 2001. "An analysis of the quasicontinuum method". *Journal of the Mechanics and Physics of Solids*, **49**(9), pp. 1899–1923.
- [20] Tadmor, E. B., Ortiz, M., and Phillips, R., 1996. "Quasicontinuum analysis of defects in solids". *Philosophical Magazine A*, **73**(6), pp. 1529–1563.
- [21] Kowalewski, O., 2005. "Theory of complex lattice quasicontinuum and its application to ferroelectrics". PhD thesis, California Institute of Technology.
- [22] Miller, R. E., and Tadmor, E. B., 2002. "The quasicontinuum method: Overview, applications and current directions". *Journal of Computer-Aided Materials Design*, **9**(3), pp. 203–239.
- [23] Kochmann, D. M., and Amelang, J. S., 2016. "The quasicontinuum method: Theory and applications". In *Multiscale materials modeling for nanomechanics*. Springer, pp. 159–193.
- [24] Dobson, M., and Luskin, M., 2008. "Analysis of a force-based quasicontinuum approximation". *ESAIM: Mathematical Modelling and*

- Numerical Analysis*, **42**(1), pp. 113–139.
- [25] Makridakis, C., Mitsoudis, D., and Rosakis, P., 2014. “On atomistic-to-continuum couplings without ghost forces in three dimensions”. *Applied Mathematics Research eXpress*, **2014**(1), pp. 87–113.
- [26] Marshall, J., and Dayal, K., 2014. “Atomistic-to-continuum multiscale modeling with long-range electrostatic interactions in ionic solids”. *Journal of the Mechanics and Physics of Solids*, **62**, pp. 137–162.
- [27] Ewald, P. P., 1921. “Die berechnung optischer und elektrostatischer gitterpotentiale”. *Annalen der Physik*, **369**(3), pp. 253–287.
- [28] Frenkel, D., and Smit, B., 2001. *Understanding molecular simulation: from algorithms to applications*, Vol. 1. Academic press.
- [29] Fennell, C. J., and Gezelter, J. D., 2006. “Is the ewald summation still necessary? pairwise alternatives to the accepted standard for long-range electrostatics”. *The Journal of Chemical Physics*, **124**(23), pp. –.
- [30] Greengard, L., and Rokhlin, V., 1987. “A fast algorithm for particle simulations”. *Journal of computational physics*, **73**(2), pp. 325–348.
- [31] Beatson, R., and Greengard, L., 1997. “A short course on fast multipole methods”. *Wavelets, multilevel methods and elliptic PDEs*, pp. 1–37.
- [32] Cheng, H., Greengard, L., and Rokhlin, V., 1999. “A fast adaptive multipole algorithm in three dimensions”. *Journal of Computational Physics*, **155**(2), pp. 468 – 498.
- [33] Tironi, I. G., Sperb, R., Smith, P. E., and van Gunsteren, W. F., 1995. “A generalized reaction field method for molecular dynamics simulations”. *The Journal of Chemical Physics*, **102**(13), pp. 5451–5459.
- [34] Gilson, M. K., Davis, M. E., Luty, B. A., and McCammon, J. A., 1993. “Computation of electrostatic forces on solvated molecules using the poisson-boltzmann equation”. *The Journal of Physical Chemistry*, **97**(14), pp. 3591–3600.
- [35] Bauer, S., Mathias, G., and Tavan, P., 2014. “Electrostatics of proteins in dielectric solvent continua. i. an accurate and efficient reaction field description”. *The Journal of Chemical Physics*, **140**(10), pp. –.
- [36] Toupin, R. A., 1956. “The elastic dielectric”. *Journal of Rational Mechanics and Analysis*, **5**(6), pp. 849–915.
- [37] Brown, W. F., 1963. *Micromagnetics*. No. 18. interscience publishers.
- [38] Müller, S., and Schlömerkemper, A., 2002. “Discrete-to-continuum limit of magnetic forces”. *Comptes Rendus Mathématique*, **335**(4), pp. 393–398.
- [39] Schlömerkemper, A., and Schmidt, B., 2009. “Discrete-to-continuum limit of magnetic forces: dependence on the distance between bodies”. *Archive for rational mechanics and analysis*, **192**(3), pp. 589–611.
- [40] Schlömerkemper, A., 2005. “Mathematical derivation of the continuum limit of the magnetic force between two parts of a rigid crystalline material”. *Archive for rational mechanics and analysis*, **176**(2), pp. 227–269.
- [41] Jha, P. K., Breitman, T., and Dayal, K., 2020. “Discrete-to-continuum limits of long-range electrical interactions in nanostructures”. *under review. Preprint: <https://www.math.cmu.edu/cna/Publications/publications2020/papers/20-CNA-020.pdf>*.
- [42] Amelang, J. S., Venturini, G. N., and Kochmann, D. M., 2015. “Summation rules for a fully nonlocal energy-based quasicontinuum method”. *Journal of the Mechanics and Physics of Solids*, **82**, pp. 378–413.
- [43] Luskin, M., and Ortner, C., 2009. “An analysis of node-based cluster summation rules in the quasicontinuum method”. *SIAM Journal on Numerical Analysis*, **47**(4), pp. 3070–3086.
- [44] Daw, M. S., Foiles, S. M., and Baskes, M. I., 1993. “The embedded-atom method: a review of theory and applications”. *Materials Science Reports*, **9**(7–8), pp. 251 – 310.
- [45] Baskes, M. I., 1992. “Modified embedded-atom potentials for cubic materials and impurities”. *Phys. Rev. B*, **46**, Aug, pp. 2727–2742.
- [46] Daw, M. S., and Baskes, M. I., 1984. “Embedded-atom method: Derivation and application to impurities, surfaces, and other defects in metals”. *Physical Review B*, **29**(12), p. 6443.
- [47] Fabri, A., and Pion, S., 2009. “Cgal: The computational geometry algorithms library”. In *Proceedings of the 17th ACM SIGSPATIAL international conference on advances in geographic information systems*, pp. 538–539.
- [48] Zapol, P., Pandey, R., and Gale, J. D., 1997. “An interatomic potential study of the properties of gallium nitride”. *Journal of Physics: Condensed Matter*, **9**(44), p. 9517.
- [49] Wright, A. F., 1997. “Elastic properties of zinc-blende and wurtzite aln, gan, and inn”. *Journal of Applied Physics*, **82**(6), pp. 2833–2839.
- [50] Jha, P. K., 2016. “Coarse graining of electric field interactions with materials”. PhD thesis, Carnegie Mellon University.